Semi-analytical modeling of the flow redistribution upstream from the mixing grids in a context of nuclear fuel assembly bow

Stanislas de Lambert, Jérome Cardolaccia, Vincent Faucher, Olivier Thomine, Bertrand Leturcq, Guillaume Campioni

Version of Record: https://www.sciencedirect.com/science/article/pii/S0029549320304349
Manuscript_93516d14994219ce43d7f2ebac3198c5
Submission to Nuclear Engineering and Design

Semi-analytical modeling of the flow redistribution upstream from the mixing grids in a context of nuclear fuel assembly bow

Stanislas de Lambert[a*], Jérome Cardolaccia[a], Vincent Faucher[b], Olivier Thomine[c], Bertrand Leturcq[a], Guillaume Campioni[d]

[a]*Université Paris-Saclay, CEA, Service d'études mécaniques et thermiques, 91191, Gif-sur-Yvette, France.*
[b]*CEA, IRESNE, Département de Technologie Nucléaire, 13108, Saint-Paul Lez Durance, France.*
[c]*Université Paris-Saclay, CEA, Service de thermo-hydraulique et de mécanique des fluides, 91191, Gif-sur-Yvette, France.*
[d]*Université Paris-Saclay, CEA, Service d'étude des réacteurs et de mathématiques appliquées, 91191, Gif-sur-Yvette, France.*

[*] *Corresponding author*

Abstract

Fuel assembly bow is a phenomenon that has drawn a significant attention over the last decades, due to its role in several issues related to nuclear core management. As a result, nuclear-based electricity production stakeholders support extensive research on this topic.

Recent studies agree that the various hydraulic forces affecting fuel assemblies over their whole height constitute a major cause of deformation. More specifically, the lateral force acting on a mixing grid strongly depends on the coolant main flow distribution between the grid itself and the surrounding water gaps. This flow redistribution varies according to the position of the assembly relatively to its neighbours. Often ignored, the modeling of the water gaps is in the limelight of this article. In order to design a simple yet accurate model of flow redistributions, we approximate the space between two successive grids (further called convergent-diffuser) as a 1D-channel. The latter is set up with suitable properties and its variable thickness reflects the deflection of the assemblies. A simple hydraulic network connecting the gap model to its adjacent grids (both represented by loss coefficients) is built to enable the flow redistribution. Successive enhancements are proposed to comply with the physical aspects neglected by the initial model.

The final version of our semi-analytical model achieved very close agreement with both CFD simulations at local scale and dedicated experimental results. The latter are obtained thanks to a mock-up made of 3D-printed grids, especially designed to validate our approach's trustworthiness. In the end, the computational efficiency of the proposed models is drawn upon to initiate a first sensitivity analysis. It aims at emphasizing the most influential inputs of the models, in order to set their values at best and obtain the most accurate description of the flow redistribution phenomena. The water gap model described in the present article is meant to be included within a larger, properly designed hydraulic network in future simulations at the scale of a full reactor core.

1 INTRODUCTION: CONTEXT AND PROBLEMATICS

The present article is intended to gain a better understanding of the underlying mechanisms behind the bow of Fuel Assemblies in the core of Pressurized Water Reactor. It represents a topic of great interest for both performance and safety of reactors of this family, with issues such as power tilt or drop times of reactivity control devices. It is also scientifically challenging as intricate multiphysical phenomena are involved. The proposed research especially focuses on forces coupling the fuel

assembly deflections to the water flow through the core (steady-state fluid-structure interaction). The fluid-structure coupling would probably explain the deformed shape of some initial cores, occuring early during the startup procedure. Starting from numerous works published over the last decade, a special attention is given to the ins and outs of flow redistribution in the vicinity of mixing grids. Basically, the fraction of the inlet flow going though the grids or through the water gaps between them is highly dependant on the width of these gaps. The related hydromechanical forces still require to be properly assessed along with uncertainty levels. The specific model built in this article will later be inserted into a more macroscopic one, necessary for running the simulations of full cores or of a selected row of fuel assemblies. To achieve this goal, a full multi-scale strategy is designed, with the main objective of providing a computationally efficient model for hydraulic forces resulting from flow redistribution. It could be used to fully characterize the fluid-structure coupling patterns originated from such phenomena through generalized sensitivity analyses. Local scale 3D simulations are provided to validate the elementary components of the model, which is then confronted to a new and specifically designed experiment.

The paper is thus organized as follows. First, a review of the existing state-of-the-art is provided, in order to fully establish the content and relevance of the proposed research. This is followed by the description of the aforementioned model for hydromechanical forces accounting for local flow redistribution, from general principles to an extended formulation presented as a generalized hydraulic network. The next two sections are dedicated to the validation of the model through comparison to both local scale simulations and experiment. The last section provides a sensitivity analysis, as a first step to obtain insights on relevant phenomena to be accounted for when modeling coupled hydromechanics for fuel assembly bow. It can also draw open perspectives for an extended application of the introduced approach to configurations of growing complexity involving several fuel assemblies.

2 REVIEW OF FUEL ASSEMBLY BOW HYDROMECHANICS AND OF THE INFLUENCE OF FORCES RELATED TO FLOW REDISTRIBUTION

2.1 Short state-of-the art for fuel assembly deformation and associated fluid-structure interaction

Deformation of fuel assemblies is an issue first reported in the 90's [Andersson, 2005]. Initial concerns arose specifically regarding IRI (incomplete rod insertion) [Andersson, 2005][Gabrielsson, 2018]. Over the last decade, the phenomenon has drawn attention for its effects on several other matters, including neutronics or core management policies [de Lambert, 2019][Gabrielsson, 2018]. The study of fuel assembly bow on an exhaustive basis is actually a very intricate task as many technical fields in nuclear engineering are involved simultaneously [de Lambert, 2019]: neutronics, thermal mechanics, and thermal hydraulics.

Three main effects are often invoked to explain fuel assembly bow: irradiation creep and growth and stationary hydraulic forces [IAEA, 2010][Wanninger, 2018]. The first two mechanisms concern the structural and material behavior of fuel assembly in operational conditions. They are out of the scope of the present article and several studies involving them can be found in the literature (see for instance [Wanninger, 2016]). Instead, the proposed work focuses on the hydraulic forces applied on the assemblies. They result from macroscopic and local flow redistributions occurring within the core, placing this research in the field of Fluid-Structure Interaction (FSI) for nuclear cores.

In this context, FSI can be seen either from a dynamical point of view, mainly in the context of seismic loadings [Ricciardi, 2009], or from a quasi-static point of view, by retaining the low-frequency component of the fluid velocity and structure deformation [Horvath, 2012]. In this paper, we focus on the latter only, as we are looking at the core deformation over one or several full operating cycles. Numerically, this problem is often treated with a partitioned two-way coupling: two solvers are used separately for each physics and, at each time step, an inner loop is performed consisting in solutions for fluid and structure problems alternatively, until convergence is reached [Benra, 2011]. Time dependence arises only due to creep processes in the fuel assemblies bow calculations and one seeks for a static fluid-structure interaction equilibrium at each creep time step. This kind of coupling induces higher computation time, and simpler models are thus necessary for both fluid and structure calculations. Studies have been pursued to develop low-cost models for the flow travelling through the nuclear core, including porous medium [Wanninger, 2018][Lascar, 2015], and hydraulic networks [Stabel, 2011]. Such models inevitably come with a series of hypotheses and assumptions over both the structural behavior and the fluid flow, needing to be confirmed or improved through dedicated studies and parametric analyses. Among those topics, the dependence of the lateral fluid forces acting on the fuel assemblies to the local flow redistributions is of primary importance. This article specifically addresses this issue through an advanced, yet computationally efficient, 1D-model of the flow pattern around and across spacer grids, validated upon both CFD and experimental data, and compatible with the requested sensitivity studies in terms of numerical cost.

2.2 Specific influence of the grids

Spacer grids located on fuel assemblies play an important role on the flow in the core. They increase the heat transfer rate from the fuel rods to the water by creating turbulent swirls and cross-flows downstream. Two important features have to be highlighted here.

First, the design of the grid outer straps (Fig. 1) significantly influences the flow behavior across the grid. Yan, in [Yan, 2014], performed calculations on a cluster of 4 quarters of assembly separated by a cross-shaped water gap, considering two types of grid straps used in the industry, respectively called ‘Design 1’ and ‘Design 2’ (Fig. 1). The study demonstrated that pressure drop and cross-flow upstream/downstream of the grids depend on the adopted design.

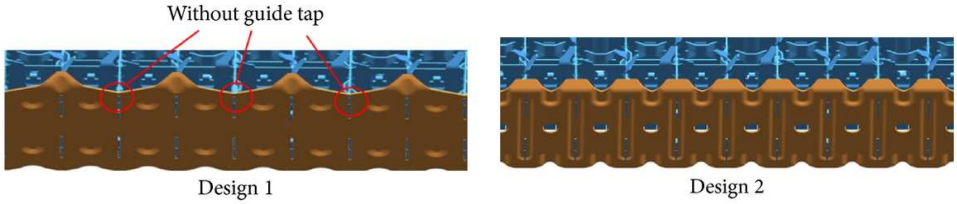

Figure 1 - Grids' outer straps as considered by Yan [Yan, 2014]

Secondly, the flow in the upstream region of the grids is subject to redistributions, especially in the case ‘Design 2’ in [Yan, 2014]. Practically, the flow can either stay in an assembly (and then cross the grid itself) or go through the bypasses (or water gaps) between the outer straps of the grids. Studies showed that this redistribution towards the bypasses depends on their width (which can vary due to bow) and on the fluid velocity [Puragliesi, 2019][Xu, 2019]. In [Bieder, 2020], the author noticed that only some extensions of the long diagonals cross flows developing within the assembly, not hindered by the control rod guide tubes, can go through the water gap. According to Bieder, the water gap acts as a barrier to inter-assembly exchanges, it tends towards isolating the flow within one assembly from each other for a 2 mm nominal width.

These aspects play a significant role in the unfolding of fuel assembly bow in an actual nuclear core. When an assembly is deflected, the widths of all the bypasses surrounding it are modified from the bottom to the top. Indeed, all spacer grids can draw closer or away from their neighbors. The flow distribution among the grids and the bypasses between them is then affected, depending on the grid geometry and the bypasses width. This globally entails differences in the pressure exerted on the opposite outer straps of one given grid, which thus yields a lateral hydraulic force of significant intensity.

2.3 Previous work introducing lateral hydraulics forces resulting from flow redistribution through the concept of added stiffness

In his experimental and modeling work, Ricciardi [Ricciardi, 2014] showed that the fuel assembly's displacement during its deformation induced velocity fluctuations in the two bypasses surrounding it. This difference of velocity brings about a pressure difference. The resulting force, depending on the displacement, is thus interpreted in terms of flow-induced added stiffness.

Then, Ricciardi [Ricciardi, 2015] proposed to estimate this effect supposing that pressure drops along the grid and the bypasses were equal. With the help of Bernoulli's principle and the Darcy-Weisbach equation, the author is able to bring out a nonlinear force depending on the fuel assembly's displacement. The simulations with this model reproduce important phenomena observed in the experiments and Ricciardi concluded that bypasses must play a key role on the dynamics of the fuel assembly. Yet, his model considers that the fluid's velocity is constant in the bypasses, and represents a fuel assembly located between two rigid walls (with larger bypasses than in a PWR context).

The force induced by the fuel assembly's displacement is thus not completely understood today in a PWR context, and recent studies neglect a fine modeling of grids' bypasses to save up simulation time. For instance, Wanninger [Wanninger, 2018] with Ruiz Antón-Pacheco [Ruiz Antón-Pacheco, 2017] considered the fuel assembly deformations by modifying the porous medium parameters; however, the pressure loss coefficient equals zero in the bypass, meaning that it does not offer any resistance to the flow in the axial direction whatever its width.

2.4 Research contribution introduced in the current paper

Starting from the state-of-the-art provided above, the goal of the present paper is to contribute to the understanding of the influence of the flow redistribution upstream from the grids on the hydraulic forces coupled to structural motion in the framework of fuel assembly bow. Some insights can be found in the work of Ricciardi who computed the added stiffness from Bernoulli's equation, but his model deals roughly with the grid geometry and neglects important phenomena regarding this local flow redistribution. A more sophisticated approach is therefore needed, based in the current article on 1D hydraulic networks applied to the configuration of interest, *i.e.* bundles of rods in the vicinity of supporting grids. The first objective is to fully describe and understand the fluid flow behavior in water gaps close to grids. The second objective is allow producing efficient simulations involving several assemblies and redistributions at a larger scale with suitable flow profiles at the core inlet and outlet, while ensuring that the relevant hydromechanical couplings are accurately reproduced.

3 STEP-BY-STEP CONSTRUCTION OF AN ADVANCED MODEL OF THE FLOW REDISTRIBUTION

3.1 Model 0: the water gap seen as a simple channel flow

The global objective is to determine the pressure field on the outer straps of two adjacent mixing grids. A natural approach thus consists in modeling the flow inside the gap between them with the so-called *extended Bernoulli equation*:

$$P_{\mathrm{A}} + \frac{1}{2}\rho V_{\mathrm{A}}^2 = P_{\mathrm{B}} + \frac{1}{2}\rho V_{\mathrm{B}}^2 + \Delta\mathbb{P} \qquad \text{(Eq. 1)}$$

where P stands for the pressure and V for the bulk velocity, subscripts A and B denote points located respectively upstream and downstream along the water gap, and $\Delta\mathbb{P} > 0$ represents the irreversible pressure loss between A and B.

Eq. 1 is actually a 1D flow model of the bypass. As such, it requires to adopt a conceptualized representation of the bypass real geometry. First, the water gap is seen as a 3D-extruded plane channel flow, whose "walls" are flush with the last rows of the two adjacent tube bundles. Then the outer strap of each spacer grid is a small protrusion in the channel, akin to speed bumps on a straight road. The guide vanes (visible on Fig. 1) provide some smoothness to this obstacle, which we represented by a bevel at the inlet and outlet of the channel. The symmetry thus created between the inlet and the outlet makes our system more similar to Design 2 in Fig. 1. The design of the mixing vanes can vary to a certain extent, and the 3D extrusion does not account for the discontinuous presence of vanes, so that in the end the angle and curvature of the bevels are uncertain quantities.

This simplified geometry is represented in Fig. 2. It consists of three different parts: a convergent C1, a straight plane channel C2 and finally a diffuser C3. We will refer to this whole flow region as the convergent-diffuser (CD) thereafter. It approximates the part of the water gap located between two spacer grids at the same level.

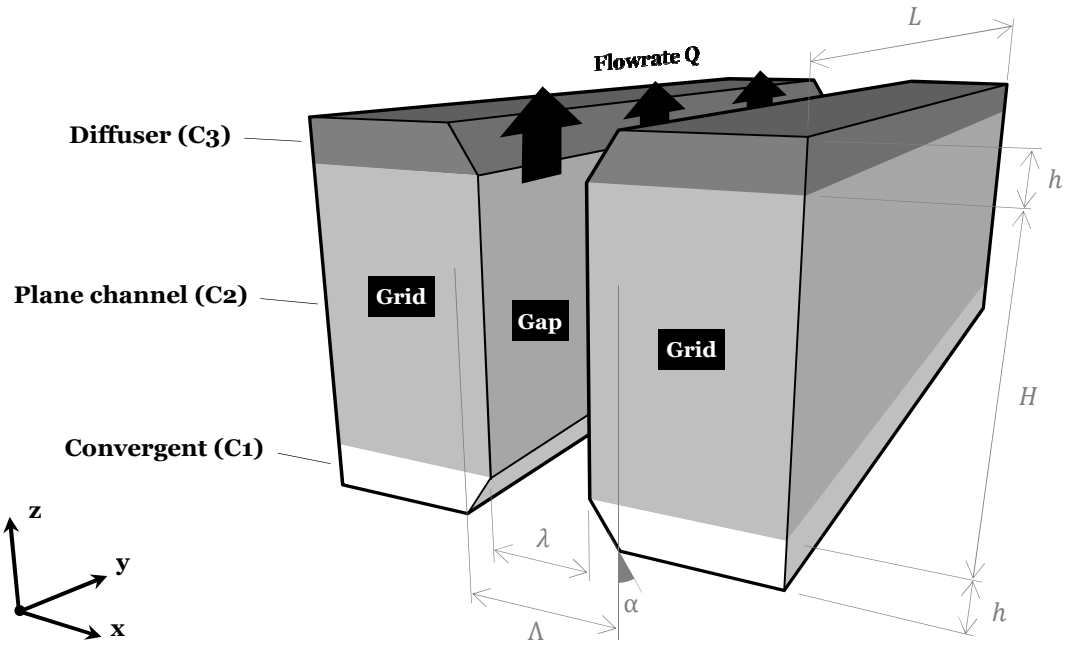

Figure 2 - Geometry considered for the area between two mixing grids

In this model, L is the grid depth (in the spanwise direction y). λ represents the channel width in C2, whereas Λ is the width of the water gap at the entrance of C1 as well as at the exit of C3. These two quantities are linked by Eq. 2 below:

$$\Lambda = \lambda + 2h \cdot \tan(\alpha) \qquad \text{(Eq. 2)}$$

where h is the height of both the convergent C1 and diffuser C3, H is the height of the middle part C2,α is the bevel angle.

The value of $\Delta\mathbb{P}$ in Eq. 1 can now be determined as the sum of pressure drops across C1, C2 and C3, for which empirical formulas are widely known [Idel'Cik, 1986]. The evaluation of these three pressure drops independently of one another is not straightforward, because H in actual grids is of the same order of magnitude as h (in other words, the velocity profile at C1 inlet may still be related to the one at C3 outlet). Even if individual empirical formulas cannot be summed *a priori* to account for the total pressure drop, CFD computations were carried out to check the validity of this approximation *a posteriori*, with quite conforming results (see section 4).

Pressure losses in hydraulic pipe systems are usually written in the following general form [Cross, 1936] (Eq. 3):

$$\Delta\mathbb{P} = KQ^a \tag{Eq. 3}$$

where K is the hydraulic resistance coefficient, Q is the volumetric flow rate, and a is an exponent depending on the used formula. The general formula presented above covers both frictional losses (*i.e.* energy dissipation per unit length due to the fluid rubbing against the duct wall) and local losses (*i.e.* energy dissipation due to sharp changes of the duct geometry).

Pressure drop across C1

In the convergent C1, we assume that the resistance is composed of both local and frictional parts. The total pressure loss across a "rectilinear converging bellmouth" is adapted from [Idel'cik, 1986]:

$$\Delta\mathbb{P}_1 = \frac{1}{2}\rho\left[\frac{\zeta_1}{(L\lambda)^2}\left(1-\frac{\lambda}{\Lambda}\right)+\frac{1}{2L^2\cos(\alpha)}\int_0^h \frac{f(\ell_1(z_1),Q)}{\ell_1(z_1)^3}\,dz_1\right]Q^2 \tag{Eq. 4}$$

where ζ_1 and f are two resistance coefficients for the local and frictional parts respectively and ρ is the fluid density.

The local gap width $\ell_1(z_1)$ is a linear map such that $\ell_1(0)=\Lambda$ and $\ell_1(h)=\lambda$. We considered that ζ_1 varied little enough on the range of commonly studied gap values $\lambda \in$ [0 mm; 20 mm] so that it could be treated as a constant. It is also common to assume that f is constant provided that the Reynolds number is high. Rather than this asumption, we retained a computational-friendly correlation from Haaland to assess f [Asker, 2014]). It yields the expression of the frictional part in Eq. 4 as the integration from $z_1=0$ to h of the Darcy-Weisbach equation applied to a pipe with a linearly varying hydraulic diameter (and thus linearly varying bulk velocity). One can check that taking f as a constant in Eq. 4 would have yielded the original Idel'Cik correlation [Rennels, 2012].

Pressure drop across C2

The middle part C2 is a plane channel of hydraulic diameter 2λ. The flow resistance is then only due to friction. The Darcy-Weisbach equation directly gives the streamwise evolution of pressure loss in C2:

$$\Delta\mathbb{P}_2 = \frac{\rho f H}{4\lambda}\left(\frac{Q}{L\lambda}\right)^2 \tag{Eq. 5}$$

Pressure drop across C3

Similarly to part C1, this resistance in the diffuser C3 depends on a local and a frictional part. The frictional resistance is equal to that of Eq. 4 by symmetry. We obtain in Eq. 6 the streamwise evolution of the pressure loss across C3 in the same way as we did for C1:

$$\Delta\mathbb{P}_3 = \frac{1}{2}\rho\left[\frac{\zeta_3}{(L\lambda)^2}\cdot\left(1-\frac{\lambda}{\Lambda}\right)^2 + \frac{1}{2L^2\cos(\alpha)}\left(\int_0^h \frac{f(\ell_1(z_1),Q)dz_1}{\ell_1(z_1)^3}\right)\right]Q^2 \qquad \text{(Eq. 6)}$$

Conclusion: total resistance coefficient of model 0

We derive the total pressure loss coefficient of model 0 from the summation of Eq. 4 to 6:

$$K_{\mathrm{CD}} = \frac{\Delta\mathbb{P}}{Q^2} = \frac{\rho}{2(L\lambda)^2}\left[\zeta_1\cdot\left(1-\frac{\lambda}{\Lambda}\right) + \frac{fH}{2\lambda} + \zeta_3\cdot\left(1-\frac{\lambda}{\Lambda}\right)^2 + \frac{\lambda^2}{\cos(\alpha)}\left(\int_0^h \frac{f(\ell_1(z_1),Q)dz_1}{\ell_1(z_1)^3}\right)\right] \qquad \text{(Eq. 7)}$$

Used to estimate lateral hydraulic forces due to pressure differences on each side of a spacer grid, this initial model turned out to significantly overestimate the forces compared to the ones observed in the literature (see for instance [Wanninger, 2018] for a set of hydraulic forces calculated in the case of a row of fuel assemblies). This originates in the neglected, and unknown, fraction of the flow passing the grids' level through the rod bundle rather than through the water gap, lowering the actual effect of the convergent-diffuser.

3.2 Model 1: distribution of the flow between the water gap and the mixing grids

In the model 0, the flow is bound to circulate in separate domains, with some kind of impermeable boundary between the rod bundles and the water gap. Water particles initially inside one fuel assembly will go through the mixing grid and remain inside the assembly downstream of the grid. Water particles initially in the water gap between assemblies will go through the bypass between grids and continue along the water gap.

In reality, when the gap width λ decreases, the flow in the bypass dries up. On the contrary, when the gap width increases enough, water rushes from the rod bundles and towards the gap. Model 1 is designed to account for these two phenomena in addition to the convergent-diffuser system of Model 0.

The grid is geometrically complex and modeling the behavior of the flow passing through it is a challenging task. Within this article, we stick to a simple expression of the irreversible pressure drop associated to the mixing grids in the following form (Eq. 8):

$$\Delta\mathbb{P}_{\mathrm{g}} = \frac{1}{2}\rho C_{\mathrm{g}} V_{\mathrm{g}}^2 = K_{\mathrm{g}} Q_{\mathrm{g}}^2 \qquad \text{(Eq. 8)}$$

where C_{g} is the coefficient of local resistance of the grid, V_{g} is the bulk velocity upstream of the half-grids, Q_{g} is the volumetric flow rate crossing one half-grid and K_{g} is the resistance given by Eq. 9:

$$K_{\mathrm{g}} = \frac{1}{2}\rho\frac{C_{\mathrm{g}}}{S_g^2} \qquad \text{(Eq. 9)}$$

with S_{g} being the flow cross-section upstream one half-grid.

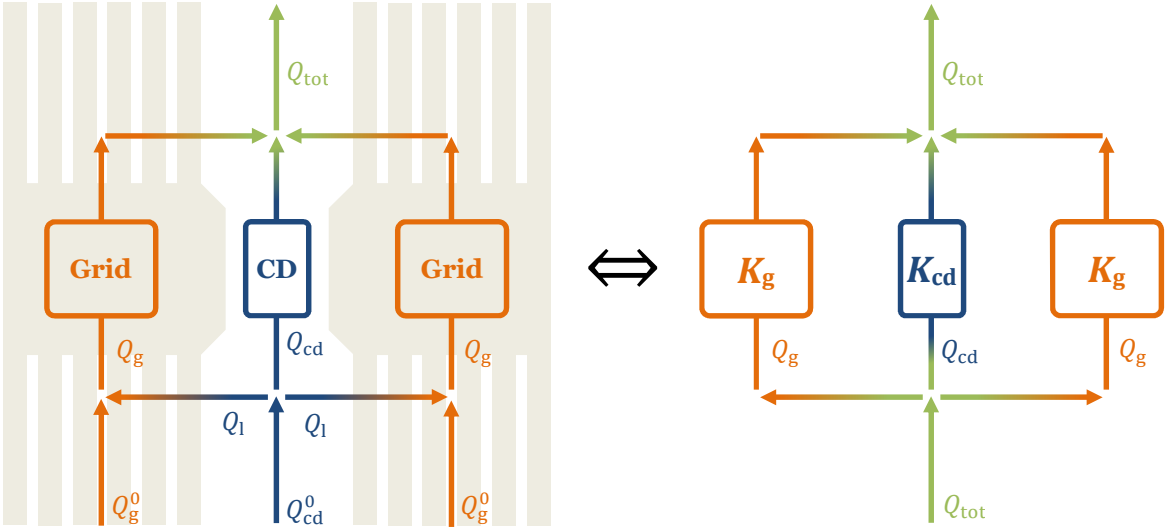

Figure 3 - Hydraulic network representing the possible pathways at the grids level (model 1)

Having developed adequate resistances for the convergent-diffuser (Eq. 7) and the grid (Eq. 9), we can set up a simple hydraulic network (Fig. 3) representing the system of interest. It consists of two half-grids separated by a convergent-diffuser (meant for the water gap). Both half-grids are supplied with the same upstream flow rate noted Q_g^0 (symmetric system), while Q_{cd}^0 is the upstream flow rate feeding into the convergent-diffuser. The leaking flow rate between the grids and the convergent-diffuser is named Q_l. The effective flow rates crossing the grids and the convergent-diffuser are respectively named Q_g and Q_{cd}. The total outgoing flow rate leaving the system is named Q_{tot}. Applying the so-called *Kirchhoff hydraulic equations* [Cross, 1936], *i.e.* the network's mass conservation and energy, we obtain the following system of equations (Eq. 10):

$$\begin{cases} \Delta P_{cd}(Q_{cd}) - \Delta P_g(Q_g) = 0 \\ Q_g^0 + Q_l = Q_g \\ Q_{cd}^0 = 2Q_l + Q_{cd} \end{cases} \quad \text{(Eq. 10)}$$

By defining $Q_{tot} = 2Q_g^0 + Q_{cd}^0$, the system can be changed into Eq. 11:

$$\begin{cases} K_{cd}Q_{cd}^2 - K_gQ_g^2 = 0 \\ 2Q_g + Q_{cd} = Q_{tot} \end{cases} \quad \text{(Eq. 11)}$$

Basically, Eq. 11 shows that the splitting of Q_{tot} into Q_{cd} and Q_g does not depend on individual inlet boundary conditions Q_g^0 and Q_{cd}^0 but on their sum only. In other words, the geometry upstream of the grids level has no influence on the redistribution computed in Model 1 (see the equivalent network in Fig. 3). Practically, when modifying Q_{cd}^0 and Q_g^0 while keeping Q_{tot} constant, the leaking flow rate Q_l will adapt so that in the end Q_{cd} and Q_g remain the same (this is the meaning of the removed equation between Eq. 10 and Eq. 11).

One can notice that the final system depends on two functions $\Delta P_g(Q_g)$ and $\Delta P_{cd}(Q_{cd})$. It is non-linear in terms of unknowns Q_g and Q_{cd}, raised to the power of a in the energy equation ($a = 2$ in our case). While an advanced algorithm could be necessary for larger non-linear systems (see for instance [Wood, 1972][Wood, 1981] or [Nielsen, 1989]), this small one can be solved easily using any root-finding algorithm. It is however shown in section 4 that the predictions of this model deteriorate when considering low values of λ. Indeed, when the CD's thickness tends towards zero, CFD simulations

show that a stagnation point appears, increasing the pressure drop in a way this model cannot reproduce, yielding the need for a second improving step in the proposed modeling strategy.

3.3 Model 2: stagnation point effect for thin water gaps

When the CD gets very narrow ($\lambda \simeq 0$), it acts as an opaque obstacle to the fluid, thus producing a stagnation point: the flow flees towards the grids, the CD upstream velocity decreases down to almost zero and the kinetic energy turns into a pressure peak at the inlet of the CD (Fig. 4).

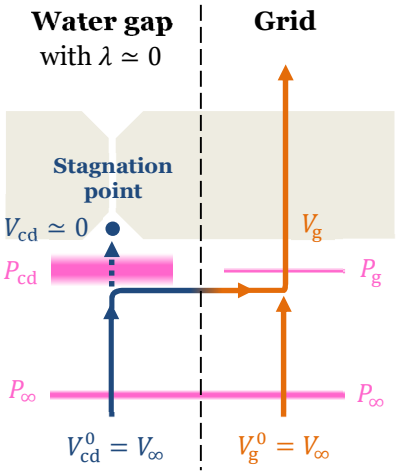

Figure 4 - Stagnation point setting up upstream from the convergent-diffuser

Therefore, we note that when λ is small enough, there is a conversion of the kinetic energy linked to V_{cd} into a kinetic energy linked to V_g. This observation introduces a 'branch-coupling' term in the energy equation.

Let us suppose that far from the obstacles, velocity V_∞ and pressure P_∞ are homogeneous (Fig. 4). As explained above, in a stagnation point context, upstream grid pressure P_g and CD pressure P_{cd} are not equal anymore. Applying the Bernoulli equation along two distinct axial streamlines across the grid and across the convergent-diffuser, we obtain Eq. 12:

$$\begin{cases} P_\infty + \frac{1}{2}\rho V_\infty^2 = P_g + \frac{1}{2}\rho V_g^2 \\ P_\infty + \frac{1}{2}\rho V_\infty^2 = P_{cd} + \frac{1}{2}\rho V_{cd}^2 \end{cases} \quad \text{(Eq. 12)}$$

which leads to:

$$\Delta P_c = P_{cd} - P_g = \frac{1}{2}\rho\left(V_g^2 - V_{cd}^2\right) \quad \text{(Eq. 13)}$$

A 'branch-coupling' term named ΔP_c appears, linking both grid and CD dynamic pressures. This additional term can be added to the equation energy (Eq. 11) in order to take into account that the pressure drops in grid and CD are no longer equal but are now shifted from each other by a value of ΔP_c:

$$\Delta P_{cd} - \Delta P_g = \Delta P_c \quad \text{(Eq. 14)}$$

Introducing the flow rates Q_g and Q_{cd}, and the cross-section S_{cd} of the CD upstream of the grids, Eq. 14 becomes:

$$K_{cd} Q_{cd}^2 - K_g Q_g^2 = \frac{1}{2}\rho\left(\frac{Q_g^2}{S_g^2} - \frac{Q_{cd}^2}{S_{cd}^2}\right) \quad \text{(Eq. 15)}$$

297 We can then define the modified resistance coefficients as below:

$$\widetilde{K}_{\mathrm{cd}}(\lambda) = K_{\mathrm{cd}}(\lambda) + \frac{\rho}{2S_{\mathrm{cd}}^2(\lambda)} \quad \text{(Eq. 16)}$$

$$\widetilde{K}_{\mathrm{g}} = K_{\mathrm{g}} + \frac{\rho}{2S_{\mathrm{g}}^2} \quad \text{(Eq. 17)}$$

298 We thus obtain the final equation system for Model 2:

$$\begin{cases} \widetilde{K}_{\mathrm{cd}} Q_{\mathrm{cd}}^2 - \widetilde{K}_{\mathrm{g}} Q_{\mathrm{g}}^2 = 0 \\ 2Q_{\mathrm{g}} + Q_{\mathrm{cd}} = Q_{\mathrm{tot}} \end{cases} \quad \text{(Eq. 18)}$$

299 One can remark that Eq. 18 (Model 2) is formally identical to Eq. 11 (Model 1), except that both
300 resistance coefficients are increased by distinct constant offsets, which entails that Eq. 11 and Eq. 18
301 will yield different solutions. This means that the flow rate redistribution is actually modified when the
302 stagnation point in taken into account (the added pressure drop is not the only outcome).

303 ### 3.4 Model 3: lateral resistance due to the rods

304 In the previous developments, the lateral obstruction due to the fuel rods presence was neglected
305 and the fluid could switch among the grid and CD channels without any resistance. This means that in
306 Models 1 and 2, the geometry upstream of the grids level has no actual influence on the flow
307 redistribution.

308 In reality, an additional lateral resistance causes the total axial pressure drop to slightly increase.
309 CFD simulations show in the next section that the bypass pressure drop computed by Model 2 is for
310 instance underestimated by approximately 10% in the case of a 1mm-thin bypass without fuel rods.
311 Practically, the next evolution of the model, *i.e.* Model 3, includes the resistance K_{l} for the leaking flow
312 rate Q_{l} coming from the bypass and going to the grid through several rows of fuel rods (see Fig. 5).

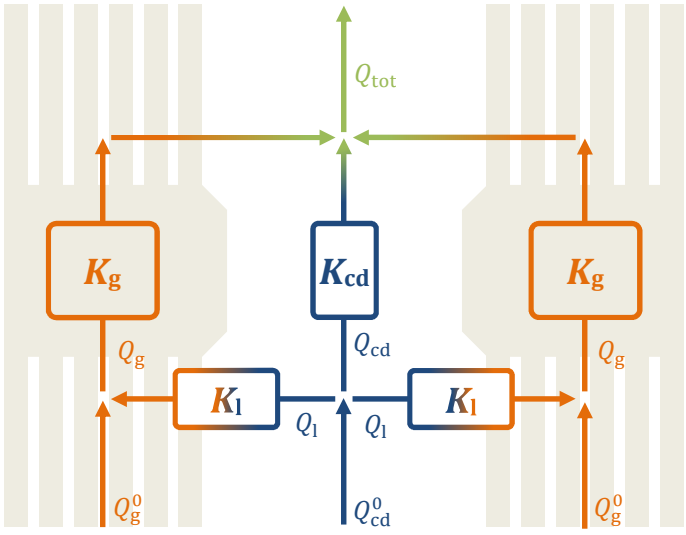

313
314 *Figure 5 – Additional lateral resistance due to cross-flows through the rod bundle (model 3)*

315 Quite intuitively, the coefficient K_{l} depends on the 3D incidence angle of the leaking flow rate in a
316 very complicated way. To provide a first approximation of this contribution, a 2D representation is
317 chosen (see Fig. 6), so that some results are available in the literature. In his work, Peybernès
318 [Peybernès, 2005][Bieder, 2015b] came up with a correlation for the lateral pressure drop across an
319 inclined rod bundle, based on the Eole experimental results. The same correlation has also been used

recently in [Wanninger, 2018] in a more global effort to estimate the hydraulic forces on PWR fuel assemblies.

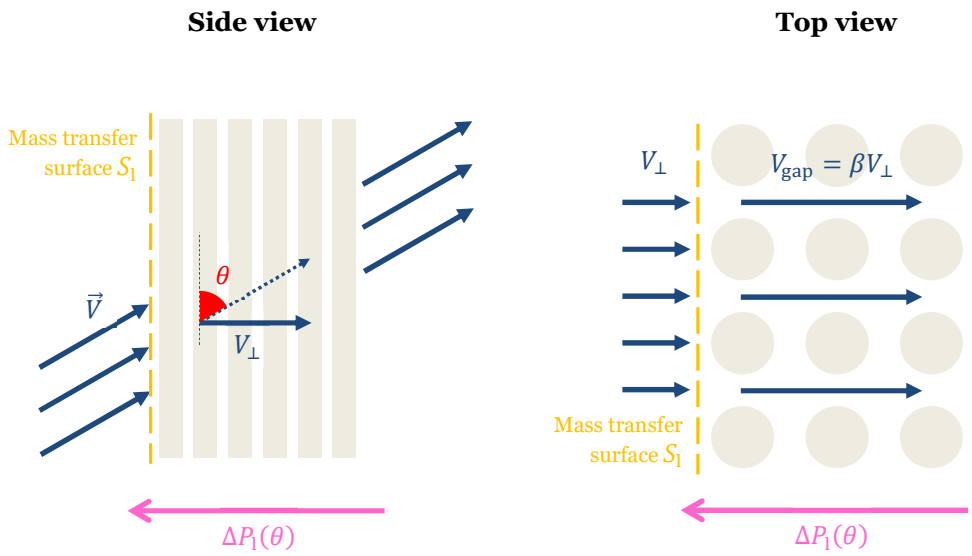

Figure 6 – General layout of an inclined flow passing through a rod bundle

The correlation states that the mean pressure drop per row is:

$$\Delta P_{row}(V_{gap}, \theta) = \frac{1}{2}\rho K_\perp \xi(\theta) V_{gap}^2 \qquad \text{(Eq. 19)}$$

where V_{gap} stands for the fluid velocity in the gaps between the rods, $K_\perp$ is the pressure drop coefficient for purely transverse flows ($\theta = 90°$) and $\xi(\theta)$ is a correction factor stemming from the Eole installation operated at various incidence angles θ, given by Eq. 20 below:

$$\xi(\theta) = \left(\frac{\sin(\theta)}{\cos\left(\frac{\pi}{4} - \frac{\theta}{2}\right)} \right)^{1.7} \qquad \text{(Eq. 20)}$$

After some computations, the resulting lateral pressure drop across N rows of fuel rods is then given by:

$$\Delta P_l(\theta) = \frac{\rho N K_\perp \xi(\theta) \beta^2}{2 S_l^2 \sin^2(\theta)} Q_l^2 = K_l(\theta) Q_l^2 \qquad \text{(Eq. 21)}$$

where β is the geometrical ratio of the gap velocity V_{gap} to the pitch velocity $V_\perp$ and S_l the lateral rectangular surface over which the fluid transfer Q_l takes place.

Writing $S_l = L h_l$ with L the total width of a fuel assembly (see Fig. 2) and h_l the corresponding height, we eventually give the following expression for K_l:

$$K_l(\theta) = \frac{\rho N K_\perp \xi(\theta) \beta^2}{2 L^2 h_l^2 \sin^2(\theta)} \qquad \text{(Eq. 22)}$$

In our context of multi-1D modeling, the incidence angle θ can be approximated from the ratio of the lateral velocity to the axial velocity in the upstream branch (*i.e.* grid or CD), which corresponds to the following expressions:

$$\theta = \begin{cases} \tan^{-1}\left(\dfrac{S_\mathrm{g}|Q_\mathrm{l}|}{S_\mathrm{l}|Q_\mathrm{g}|}\right) & \text{if } Q_\mathrm{l} < 0 \\ \tan^{-1}\left(\dfrac{S_\mathrm{cd}|Q_\mathrm{l}|}{S_\mathrm{l}|Q_\mathrm{cd}|}\right) & \text{if } Q_\mathrm{l} > 0 \end{cases} \quad \text{(Eq. 23)}$$

Using the newly added resistance to lateral flow, system (Eq. 18) becomes:

$$\begin{cases} \widetilde{K}_\mathrm{cd} Q_\mathrm{cd}^2 - \widetilde{K}_\mathrm{g} Q_\mathrm{g}^2 - K_\mathrm{l} Q_\mathrm{l}^2 = 0 \\ 2Q_\mathrm{g} + Q_\mathrm{cd} = Q_\mathrm{tot} \\ Q_\mathrm{g}^0 + Q_\mathrm{l} = Q_\mathrm{g} \end{cases} \quad \text{(Eq. 24)}$$

Unlike in previous models, the inlet flow rate Q_g^0 (or Q_cd^0) now plays an important role in the redistribution of Q_tot between Q_g and Q_cd, due to the presence of Q_l in the first equation of system (Eq. 24). This means that in Model 3, the geometry of the fuel assemblies upstream of the grids does have an influence on the redistribution. In practice, this is shown by the appearance of several new geometrical parameters, notably β, h_l and N. The value of β can be easily calculated given the pitch and diameter of fuel rods. However, h_l and N characterize the dimensions of the region where cross-flows take place between the water gap and the grids. As such, those two parameters are complex to estimate and are likely to depend on the bypass thickness λ.

4 COMPARISON WITH LOCAL CFD SIMULATIONS

4.1 Presentation of the CFD models

CFD simulations are carried out in order to validate our semi-analytical model. The local-scale solutions provided by two different programs, namely TrioCFD [Angeli, 2015] and Code_Saturne [Archambeau, 2004], are cross compared to produce reliable reference data.

The geometry considered for the calculations is shown on Fig. 7. It consists in two assemblies separated by a central bypass of adjustable thickness λ (1, 2, 3, 5, 10 and 20 mm). Two rods are represented along the y-axis while there are four and a half rods per assembly along the x-axis. The convergent-diffuser area is modelled as shown in Fig. 2 (i.e. 3D extruded), but the nearer fuel rods go through parts C1 and C3. In this way, a notch is set up around the fuel rod positions. Thus, the outer straps geometry created comes closer to 'Design 2' (i.e. to a real grid design). The tube bundle regions use a rather fine mesh and the intricate geometry of the grids is not reproduced. Instead, we use a porous media approach with a coarser mesh and calibrate the source term in order to reach exactly the desired value of K_g. For the same reasons, some volume inside the grids close to the convergent-diffuser is not meshed (see again Fig. 7), since it would bring unwanted recirculations in the flow, thus increasing artificially the value of K_g.

The mesh is unstructured, consisting in 3D tetrahedral elements with two prismatic layers applied on surfaces with a no-slip boundary condition (fuel rods and outward faces of the grids, see Fig. 7). As TrioCFD does not allow prismatic volumes, a specific version of the mesh was created where the prisms near the walls are split into five tetrahedrons.

A mesh convergence study has been realized for the case $\lambda = 5$ mm. For both codes, four calculations have been run with various grid refinements whose y^+ averaged on wall surfaces always laid in the $[30; 100]$ range required by the wall function. Volumetric flow rates in the water gap and pressure drop across the grid exhibited deviations of less than 6% between all the meshes. We selected

the second thinnest mesh considering it was a fair trade-off between accuracy and performance. It contains approximately 5.10^6 cells.

Symmetry boundary conditions are applied on each lateral side of the fluid domain (see Fig. 7). Inside the grids, a symmetry condition is applied on all the lateral surfaces (which are mainly fuel rods) in order to disable friction that would otherwise increase the pressure drop artificially (K_g is defined explicitly as a source term, see above). Outside of the grids, a no-slip condition is applied on the fuel rods and on the convergent-diffuser walls (Fig. 7). An axial flow velocity of 6 m/s is imposed uniformly on the bottom inlet surface (the Reynolds number based on bulk velocity and rod diameter is 10^5). Finally, a constant pressure is set on the top outlet surface (see Fig. 7).

Turbulence is handled by a standard k-ε RANS model accompanied by a wall function (1-scale model - log law for Code_Saturne and Richardson for TrioCFD). We aim at reaching a steady state. This turbulence model could have difficulty computing accurately the transverse flows. However studies based on large eddy simulations (LES) and two experiments, AGATE [Bieder, 2014][Bieder, 2015a] and MATHYS_H [Bieder, 2012], have shown that the k-ε model can reproduce the coolant behavior near the mixing grid where the flow is mainly advection-controlled. More recently, Bieder also pointed out that conclusions pulled from LES and k-ε calculations on an inter assembly setup were similar [Bieder, 2020]. Dedicated LES calculations are considered as prospects in the future, but at this time those results encouraged us to use the k-ε model for our CFD simulations.

Water density is 700 kg/m3, close to the operating value in a PWR.

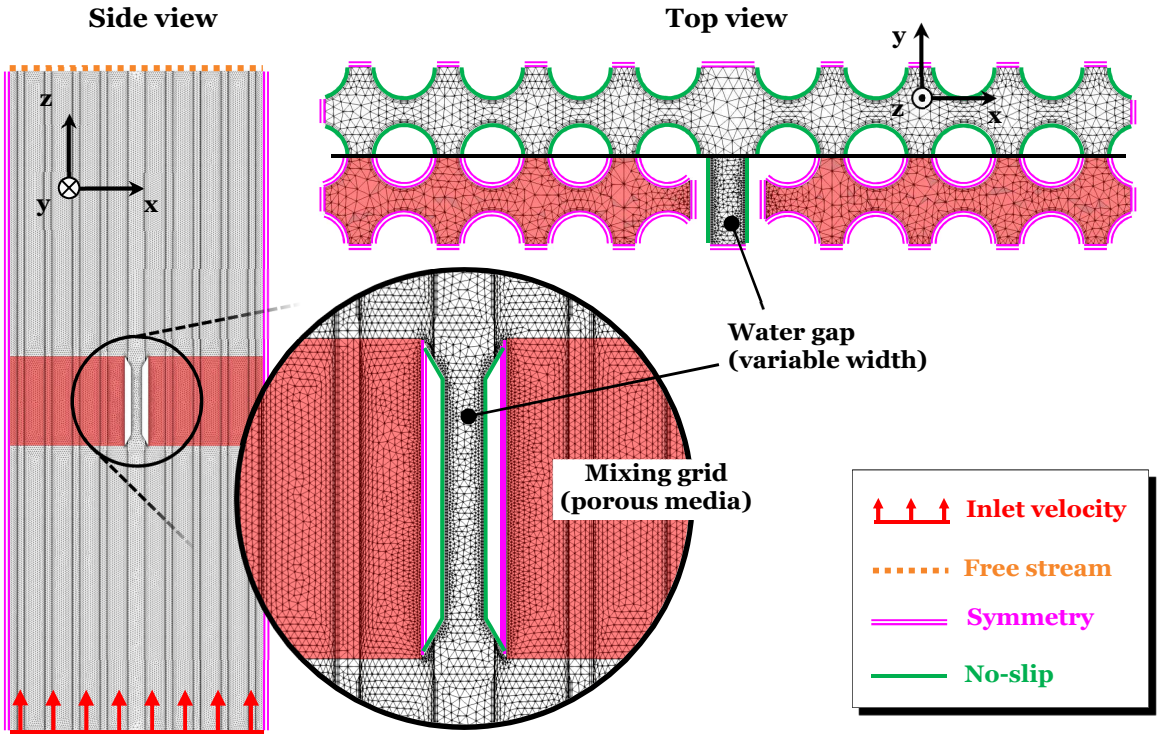

Figure 7 – Description of the mesh (λ = 5 mm here) and boundary conditions used in the CFD simulations

4.2 Pressure drop across the grids

The first physical value of interest is the pressure drop across the convergent-diffuser. Two different locations were probed, respectively called 'middle' and 'bevel' (Fig. 8). The pressure drops obtained for the different CD thicknesses are plotted on Fig. 9.

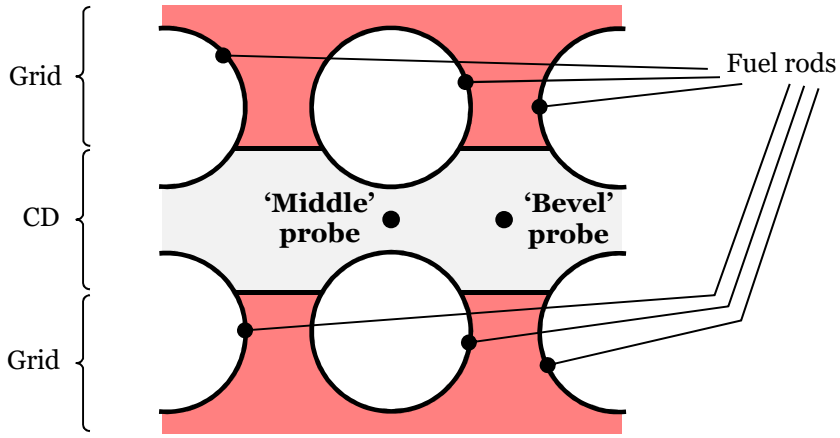

Figure 8 - Position of the probes of pressure drop

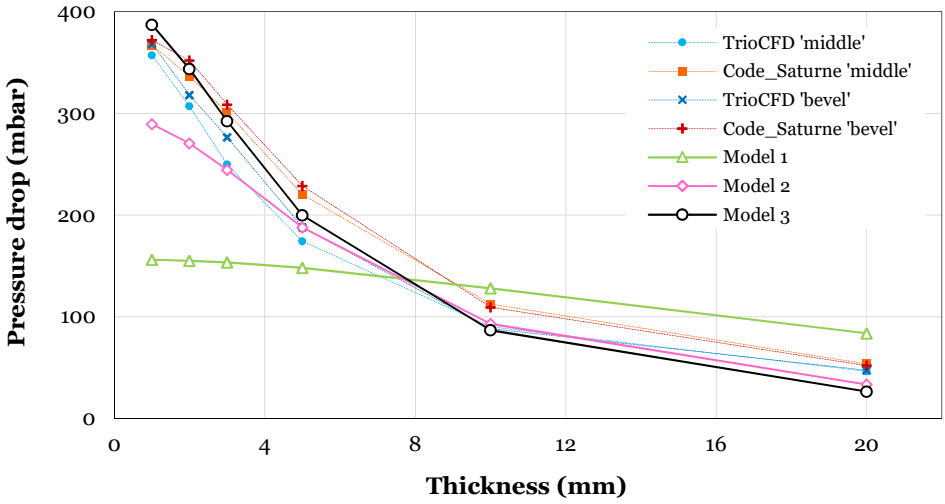

Figure 9 - Pressure drop as a function of the water gap thickness

Both CFD codes found that the pressure drop is almost the same for the 'middle' probe and for the 'bevel' probe. This means that the pressure hardly varies in the spanwise direction.

Compared to CFD, Model 1 shows poor results below $\lambda = 6$ mm. As mentioned in section 3, this discrepancy is related to the stagnation point at the entry of the CD (clearly visible in Fig. 10 showing TrioCFD results in mid-plane for $\lambda = 1$ mm) but not taken into account in the model. Model 2 logically performs better, with a relatively good agreement with both CFD reference results, even though a 25% deviation could be underlined for the smallest values of λ. Finally, Model 3 yields excellent results for all values of λ between 1 and 20 mm, with the internal parameters given in section 6.3.

It is worth putting emphasis on the CPU cost associated to one data point of Fig. 10, reaching several days in the case of CFD versus a split second in the case of the semi-analytical Model 3 (for basically the same results).

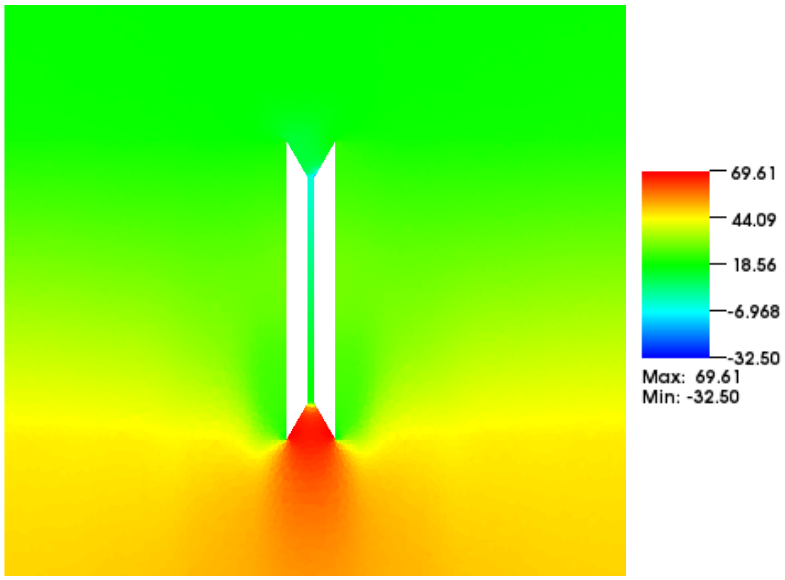

Figure 10 - Pressure peak underneath the CD for $\lambda = 1$ mm

4.3 Flow rate and mean axial velocity

In this section, flow rate and velocity in the water gap obtained with CFD are compared to those given with the proposed semi-analytical models (see Fig. 11). Since the mesh for CFD simulations only contains two rows of rods along the y-axis (see Fig. 7), the flow rate must be rescaled to match the grid length L used in the models (see Fig. 2).

Fig 11a shows that Model 1 fails to reproduce the correct slope for the flow rate, but Models 2 and 3 give quantitatively accurate results. Model 3 stands out for its ability to stick to CFD curves even for the smallest values of λ (below 3 mm).

The bulk velocity in the bypass is plotted on Fig. 11b. When λ increases starting from very small values, a maximum is reached for $\lambda \simeq 3mm$ and the bulk velocity decreases thereafter. Model 1 does not reproduce this phenomenon as the bulk velocity keeps increasing with the bypass thickness. The modification brought in Model 2 (branch coupling term for capturing stagnation points) is the key to capturing the physics correctly. In this case, again Model 3 allows to further tune the solution for small values of λ to get very close to the reference curves.

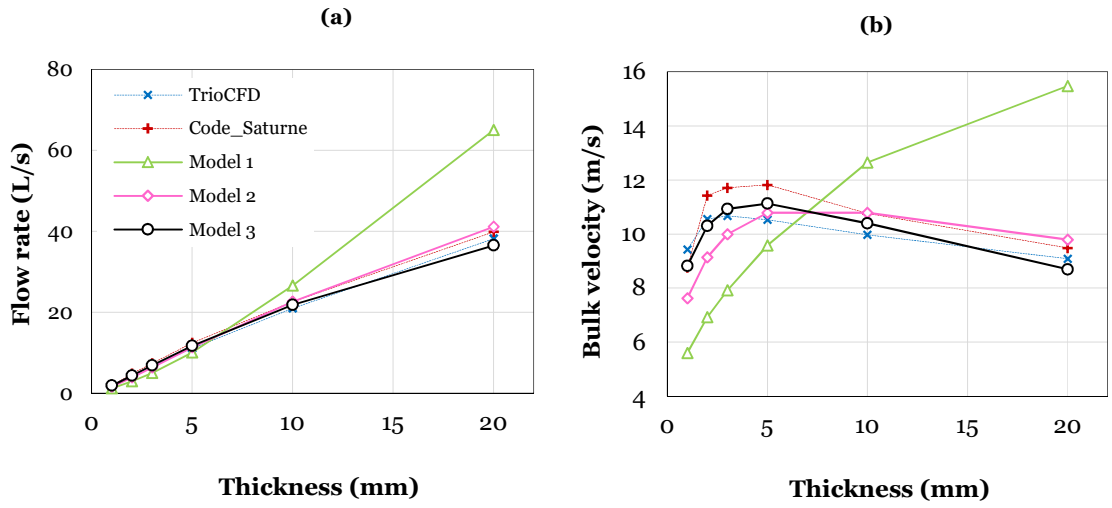

Figure 11 - Flow rate (a) and axial mean velocity (b) as a function of the water gap thickness

4.4 Advanced calibration for parameters of Model 3

As mentioned in Section 3, Model 3 (*i.e.* integrating a resistance to the leaking flow Q_l) requires two empirical parameters to be set, namely the number of fuel rod rows N and the height h_l involved in the leak flow.

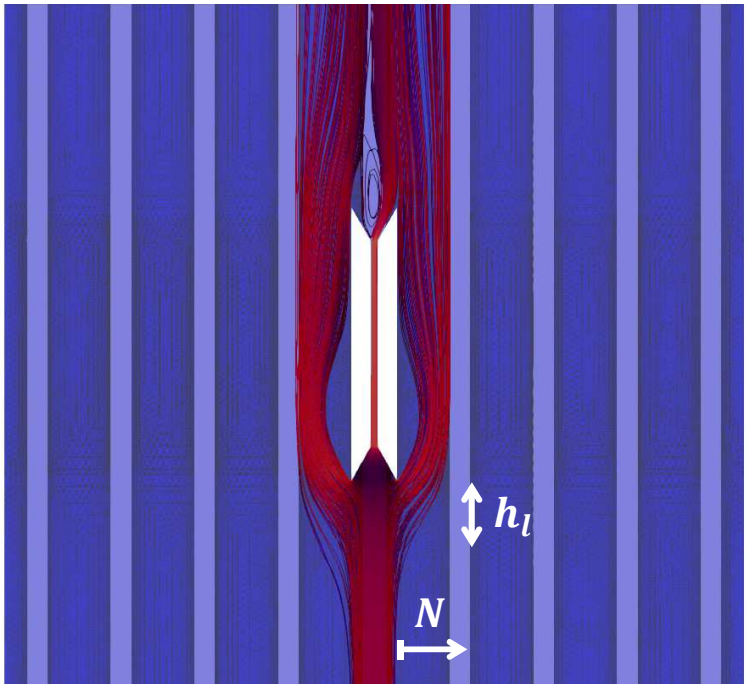

Figure 12 - Streamlines in the water gap for $\lambda = 1$ mm

First qualititative insights regarding these parameters are given by the streamlines in the vicinity of the grid for the flow coming initially from the water gap inlet boundary. An example is provided in Fig. 12 for the streamlines obtained from the Code_Saturne simulation with a gap width $\lambda = 1$ mm. For this configuration, the redistribution (from the bypass to the grids) is initiated at a very small distance h_l upstream of the obstacle. Furthermore, the fluid enters only the first row of the rod bundle inside the grids, yielding $N = 1$ in this particular case.

A more generic and quantitative approach is to calculate the lateral flow rate for successive rows upstream of the grids. The flow rates are calculated the same way as Yan [Yan, 2014]: clip planes are created parallel to the water gap for the first three rows and each of them is cut into several sub-surfaces along the bundle direction to estimate the evolution of the computed flow rates (see Fig. 13 for the details). The first sub-surface is located between 0 and 5 mm upstream from the grids, and so on for the next 5 up to 30 mm upstream, with a 5 mm height each. The seventh and last sub-surface represents the lateral flow rate through the remaining geometry (between 30 mm and the 150 mm in the upstream direction).

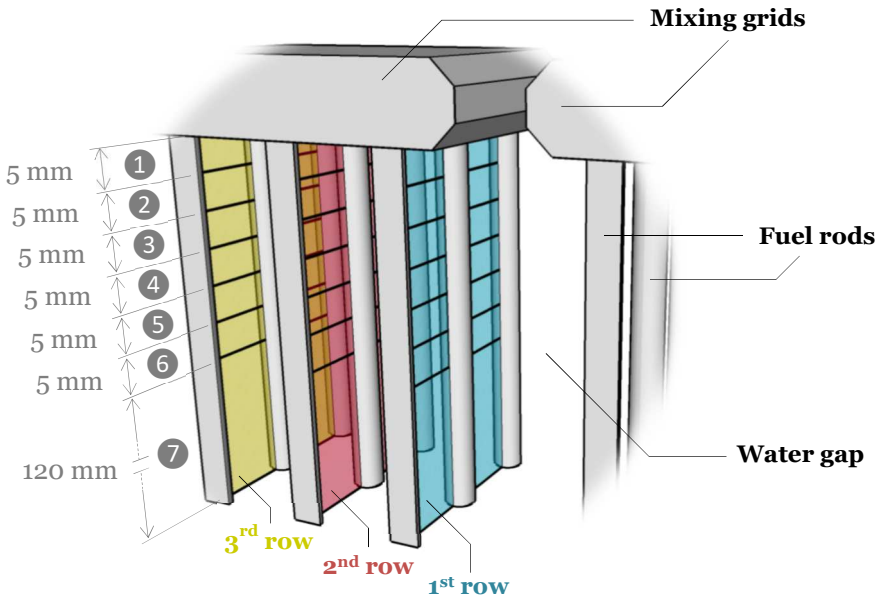

Figure 13 – Clip planes used for post-processing of local lateral flow rates and subdivision into sub-surfaces

This post-processing has been applied to the simulations performed with TrioCFD, for the two extremum values of CD's thicknesses (*i.e.* $\lambda = 1$ and $\lambda = 20$ mm) and the first three rows of fuel rods.

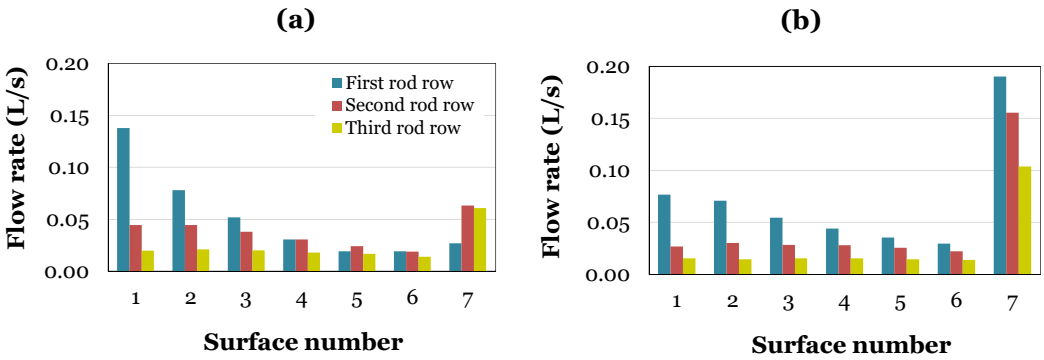

Figure 14 - Lateral flow rates calculated for a water gap width of (a) 1 mm and (b) 20mm

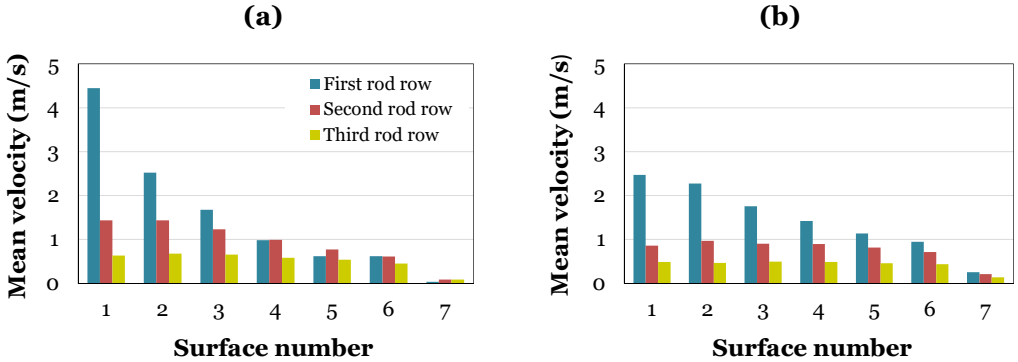

Figure 15 - Lateral average velocity for for a water gap width of (a) 1 mm (b) 20 mm

Fig. 14 and 15 show the resulting flow rates and lateral average velocities respectively for both considered values of the water gap width. Absolute values are displayed for the sake of clarity in the

comparisons, even though the fluid goes from the assembly to the bypass for the larger values of the water gap and in the opposite direction otherwise. The redistribution in the 1 mm-case (Fig. 14a and Fig. 15a) is strong near the grid (in agreement with what was observed on the streamlines of Fig. 12), and for the first row of fuel rods. Actually, 60% of the total lateral flow rate occurs through surfaces 1 and 2 (*i.e.* within the first centimeter below the grid) and for the first rod row only. The lateral average velocity is also quite important within the first millimeters (almost the same order of magnitude as the axial velocity), but drops quickly under 1 m/s after only 1,5 cm. The 20 mm-case (Fig. 14b and Fig. 15b) shows smaller flow rates and they are more spread on all sub-surfaces. Only 30% of the total lateral flow rate is located within sub-surfaces 1 and 2 for the first row and the lateral velocity in the vicinity of the grid is again significantly larger for the first row of rods.

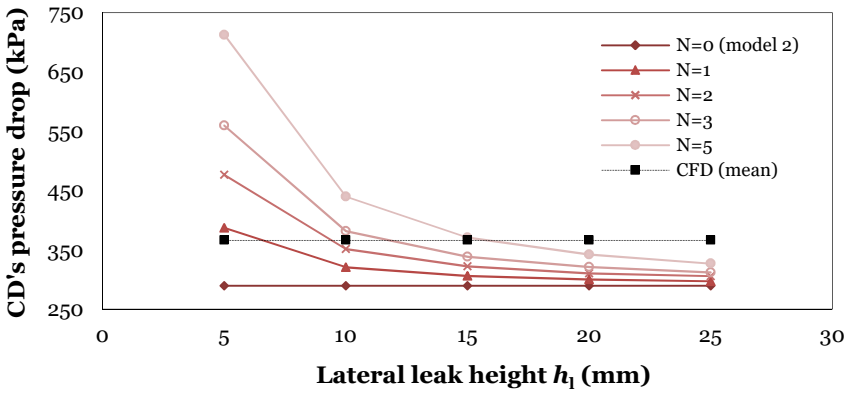

Figure 16 - Pressure drop as a function of leak length (for several row numbers) when λ = 1 mm

To close this section, it is noticeable that parameters h_l and N cannot be chosen independently. Fig. 16 plots the pressure drops in the CD determined by Model 3 for many different combinations of leak height h_l and number of rows N, as well as the reference value computed by CFD: several couples of values provide a good match, for instance $(h_l = 5\text{ mm}\,;N = 1)$, $(h_l = 11\text{ mm}\,;N = 3)$ or $(h_l = 15\text{ mm}\,;N = 5)$. The first one is probably the most relevant for small widths λ, while the second one best describes the configurations where λ is large. However, it is still possible to keep constant values for h_l and N for all values of λ. The sensitivity analysis in Section 6 will help to assess the influence of these choices on the results produced by the semi-analytical models.

5 COMPARISON WITH DEDICATED EXPERIMENTAL RESULTS

5.1 Experimental mock-up

In order to check that the previous semi-analytical models provide physically relevant results (in terms of pressure drop and flow rate distribution between the grids and the CD), a specific experimental setup was designed, named DIVA+G. The detailed description of the tests goes beyond the scope of the current article and will be subject to its own publication process. Two half grids were 3Dprinted in plastic material. They consist of a thick plate filled with numerous holes arranged in a triangular pattern, allowing a controlled pressure drop while maintaining flow conditions as homogeneous as possible. The space between the half-grids uses the same simplified geometry for the water gap as the theoretical model described in Section 3 (Fig. 2). Several shims of various thicknesses allow modifying the distance between the half-grids (*i.e.* the water gap). All these elements are placed in the test section of an hydraulic loop (Fig. 17).

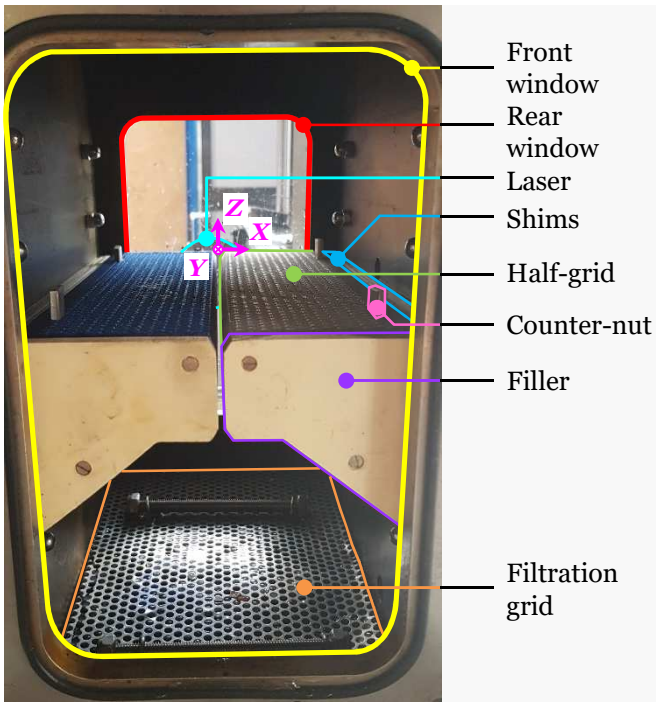

Figure 17 – The DIVA+G mock-up

Two differential pressure probes are located on a side wall at the base of one of the grids, above and below it. The local mean axial velocity is measured thanks to Laser Doppler Velocimetry. Between 60 and 340 locations are probed, according to the water gap width. This allows determining accurately the flow rate through the gap, and therefore the flow rate within the grids by difference with the total flow rate.

5.2 Parameters of models 1 and 2 for DIVA+G

In DIVA+G, metallic shims are successively added aside to put grids closer. As a result, the ratio between flow cross-sections inside the grids and at the inlet decreases as the water gap goes thinner. Using the correlation in [Idel'Cik, 1986] for thickened grids, we are able to match the pressure drop measurement when the gap is closed ($\lambda = 0$). By extrapolation, it is possible to express the coefficient of local resistance C_g (defined in Eq. 8) with the following relation (Eq. 25):

$$C_g(\lambda) = 4.23 - 0.06\lambda \qquad \text{(Eq. 25)}$$

Here λ stands for the average width of the water gap, in millimeters. Likewise, the flow cross-section upstream of one half-grid S_g can be evaluated thanks to the following equation (Eq. 26):

$$S_g(\lambda) = \frac{1}{2}(S_0 - L\lambda) \qquad \text{(Eq. 26)}$$

where S_0 is the mock-up's cross-section (see Fig. 17). As mentioned above in the article, the pressure loss associated to crossing the grids is thus given by (Eq. 27):

$$\Delta P_g = K_g(\lambda) Q_g^2 = \frac{1}{2}\rho C_g(\lambda)\frac{Q_g^2}{S_g(\lambda)^2} \qquad \text{(Eq. 27)}$$

Those functions are used to compute the solution for both Model 1 and Model 2. Model 3 is obviously out-of-scope in this section since no rods are included in the DIVA+G mock-up.

5.3 Comparison to DIVA+G results

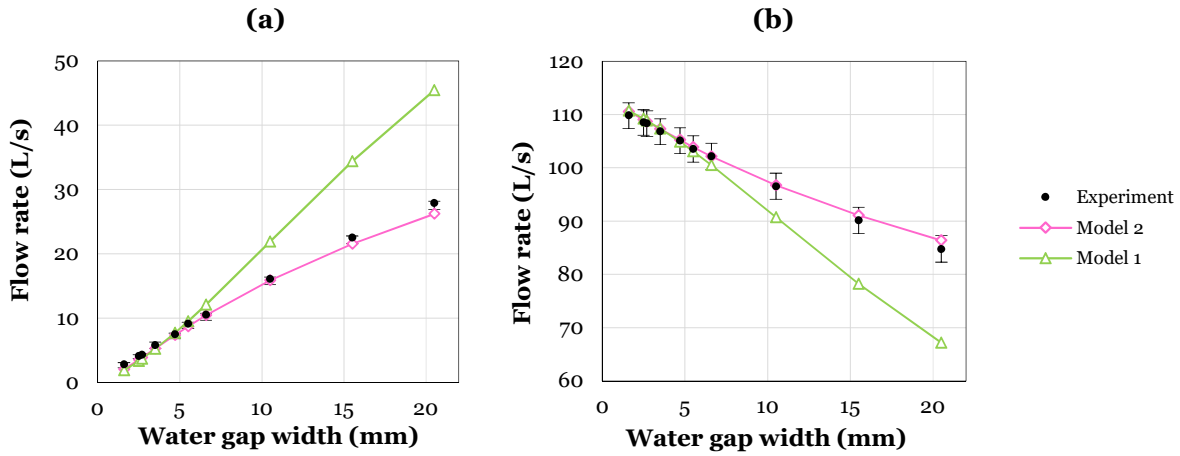

Figure 18 – Models vs DIVA+G: flow rates in (a) the water gap and (b) the grids (uncertainty ranges are plotted over experimental points)

Fig. 18 represents the volumetric flow rate in the CD (a) and in the grids (b) as a function of λ. Model 2 is in very good agreement with experiments, whereas Model 1 shows significant discrepancies for larger gaps, confirming the importance of the stagnation point modeling to account for the heterogeneity of the pressure field.

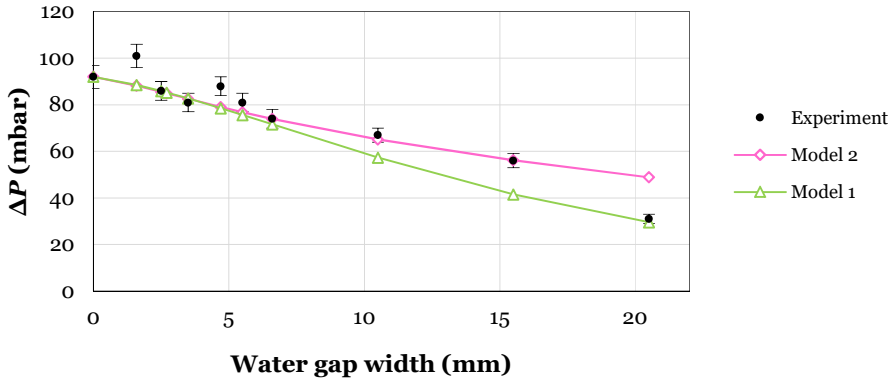

Figure 19 - Models vs DIVA+G: pressure drop, absolute uncertainties are indicated over measurements' points

Finally, Fig. 19 presents the pressure drop through the grids. In DIVA+G, this value is obtained through the two pressure sensors placed on both sides of the right half-grid (see Fig. 17). Experimental measurements are here subjected to additional uncertainties probably due to non uniform operating conditions in the loop over the complete test sequence stretching over one week approximately (see for instance the points for values of λ of 1.6 mm, 4.5 mm and 20 mm). However, both Models 1 and 2 accurately reproduce the decrease of the pressure drop through the grid with the opening of the water gap.

As a conclusion, the very good match between Model 2 and DIVA+G experimental data (in terms of pressure drop and flow rates) is remarkable, all the more so as this version of the semi-analytical model needs no empirical parameter at all. It shows that the physics of the redistribution upstream of the grids is correctly understood and well captured by our semi-analytical models.

6 SENSITIVITY ANALYSIS OF THE MODELS

This last section provides some early work illustrating the potential of the proposed semi-analytical approach in terms of advanced sensitivity analysis, made possible by the balance between accuracy for the phenomena of interest and computational efficiency. Two case studies are considered: first, the sensitivity of Model 2 results to variations of its internal parameters together with some of the DIVA+G experimental inputs, and second, a deeper dive into the inner workings of the ΔP_c and ΔP_l corrective terms resulting from the stagnation point modeling, through compared sensitivity analyses of Model 2 and Model 3.

6.1 Model 2 (applied to the DIVA+G experiment)

In order to analyze the sensitivity of Model 2 and the experiment's parameters, 100 000 calculations were performed thanks to CEA's Uranie uncertainty platform [Gaudier, 2010] with different values of input parameters (see Section 3) to estimate the Sobol Indexes [Jacques, 2011][Iooss, 2011]. The sampling is operated by a Latin hypercube method [McKay, 1979]. The different inputs are drawn from uniform distributions whose bounds are detailed in Table 1. In Section 5, it was explained why the grid coefficient C_g of the DIVA+G mock-up was a linear function of the water gap width λ. However, in order to make the sensitivity analysis simpler [Iooss, 2011], we act as if these two variables were uncorrelated.

Input	Minimum	Maximum	Comments
$\boldsymbol{\lambda}$	0.1 mm	20.5 mm	
$\boldsymbol{H}, \boldsymbol{h}, \boldsymbol{\alpha}$	−10%	+10%	(Λ/λ) thus varies up to $\pm$20% for $\lambda = 1$ mm and $\pm$ 5% for $\lambda = 20$ mm (this ratio plays a major role on the flow redistribution, see Eq. 7)
$\boldsymbol{\zeta_1}$	0.1	0.6	+20% upper margin w.r.t. the sudden contraction ($\zeta_1 = 0.5$ when $\alpha = 90°$)
$\boldsymbol{\zeta_3}$	1	1.3	$\zeta_3 = 1$ is for a sudden expansion ($\alpha = 90°$), $\zeta_1 = 1.15$ the nominal value
$\boldsymbol{C_g}$	3.00	4.23	C_g depends on λ (see section 3)
$\boldsymbol{Q_{tot}}$	−10%	+10%	
$\boldsymbol{\rho}$	997 kg.m^{-3}	1000 kg.m^{-3}	Temperature variation between 5°C and 25°C
$\boldsymbol{\mu}$	8 × 10^{-4} Pa.s	1.5 × 10^{-4} Pa.s	Temperature variation between 5°C and 25°C
$\boldsymbol{\varepsilon}$	1 µm	100 µm	$\varepsilon = 1$ µm is typical steel, $\varepsilon = 100$ µm is an upper bound for 3D-printed PETG (ε is the wall rugosity, appearing in Haaland formula for f [Asker, 2014])
$\boldsymbol{S_0 = L \times W}$	−1 mm × −1 mm	+1 mm × +1mm	

Table 1 - Inputs for sensitivity analysis of model 2 in the context of DIVA+G experiments

The chosen outputs of interest are the volumetric flow rate fraction going through the water gap, *i.e.* Q_{cd}/Q_{tot}, as well as the pressure drop divided by the square of total flow rate, *i.e.* $\Delta P_g/Q_{tot}^2$. Such nondimensionalization prevents any undesirable variation of Q_{cd} and Δp_g which would be imputed solely to an increase or decrease of the total flow rate Q_{tot} going into the system.

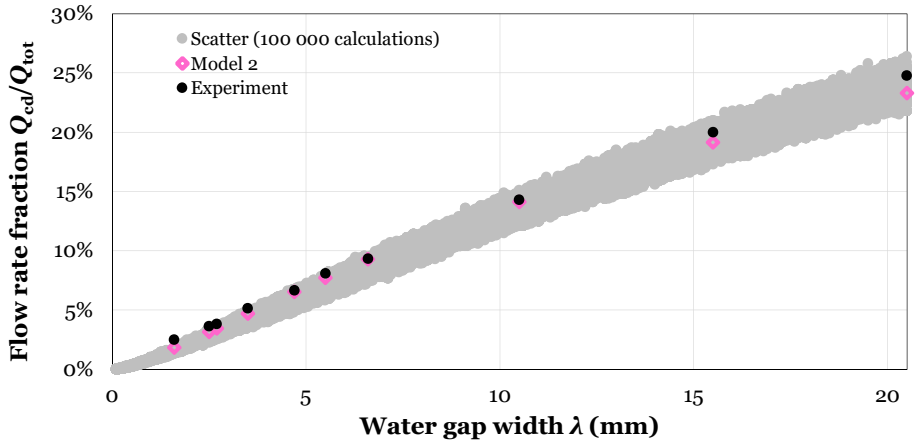

Figure 20 – Flow rate in the CD computed with perturbed input parameters

Fig. 20 represents the nondimensional flow rate in the CD, for both experimental, initial Model 2 calculation (with nominal values), and the 100 000 calculations results. It highlights that whatever the draw, the maximal relative deviation towards experimentation is around 20%. Keeping in mind that every single possible input variable has been considered and that they have been drawn uniformly in the whole range of admissible values, this is a very satisfactory result. First, it shows that a rational change in the models' parameters will keep the solution (in terms of flow rate) in an acceptable range. Second, the distribution of the scattered results around the experimental values shows some robustness regarding the measurement errors. Finally, the shape of the scatter plot suggests that the flow rate is mostly a function of the thickness.

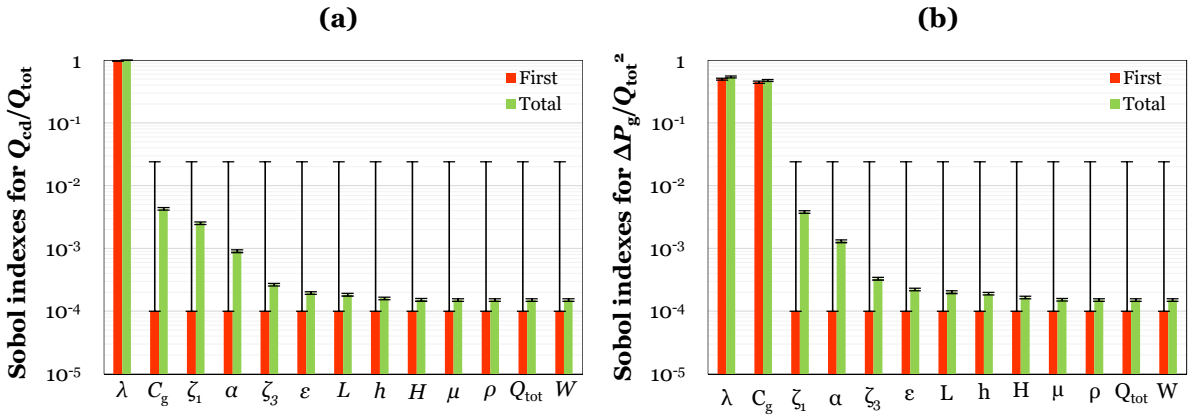

Figure 21 – Sobol indexes and 95% confidence intervals for Q_{cd}/Q_{tot} (a) and $\Delta P_g/Q_{tot}^2$ (b) obtained with 100 000 calculations with Model 2 in the context of DIVA+G experiments

To explicitly quantify the influence of the modeling parameters on the variation of Q_{cd}/Q_{tot}, first and total Sobol ([Jacques, 2011] or [Jacques, 2006] in English) are computed and displayed in Fig. 21a. The first index associated to the thickness λ is indeed around 1. It means as anticipated in Fig. 20 that the output can be considered in first approximation as a function of λ only, neglecting some small interactions with other inputs. Confidence intervals of the other inputs for the first index are too large to be discussed. However, according to the total indexes (whose confidence intervals are small enough to allow interpretation), one could see that C_g, ζ_1 and α are the next three more influential inputs on the prescribed ranges, after the thickness λ. There is no way to tell if those parameters step in alone or through their interactions, but their total effect stands out from the others. More specifically, caution

must be exercised with regards to C_g, as it was considered independent of λ to compute the Sobol indexes, whereas analyses from DIVA+G experimental campaign clearly concluded that these two parameters were strongly related (as such they should be considered as a same group of inputs [Jacques, 2011]). Further correlation analyses could be performed to highlight this topic, but this goes beyond the scope of the current paper.

Fig. 21b indicates the Sobol indexes calculated for the output $\Delta P_g/Q_{tot}^2$. The remarks pointed out above are still relevant, and the four more influential inputs are the same. The difference is that the effect of C_g is much more important in this case (see the total and first indexes) because the pressure drop is directly proportional to the loss coefficient.

6.2 Model 3 (and comparison to the simpler Model 2)

The common distinctive feature of Model 2 and Model 3 is held in the ΔP_c corrective term, and Model 3 then stands out from Model 2 for the additional parameters introduced by the lateral resistance K_l. It is interesting to analyze the sensitivity of $\Delta P_c = P_{cd} - P_g$ to different values of new inputs associated with K_l and to compare with Model 2's conclusions discussed above. Building on the results of Fig. 21, every parameter whose influence seemed negligible are now considered as constants. Simulations are otherwise analog to the ones performed in section 5. For Model 3, the inputs of the sensitivity analysis are listed in Table 2.

Input	Minimum	Maximum	Comments
$\lambda^{(*)}$	1 mm	20 mm	
$C_g^{(*)}$	0.9	1.3	
μ	10^{-5} Pa.s	10^{-4} Pa.s	Used to calculate the local Reynolds number in $K_\perp$ (Eq. 22)
N	1	3	See Fig. 12
h_l	1 mm	100 mm	Linear probability density function (instead of uniform) in order to promote low values of h_l (see Fig. 12)

Table 2 - Inputs for sensitivity analysis of Model 2 ($*$ only) and 3 in the context of real PWR fuel assemblies

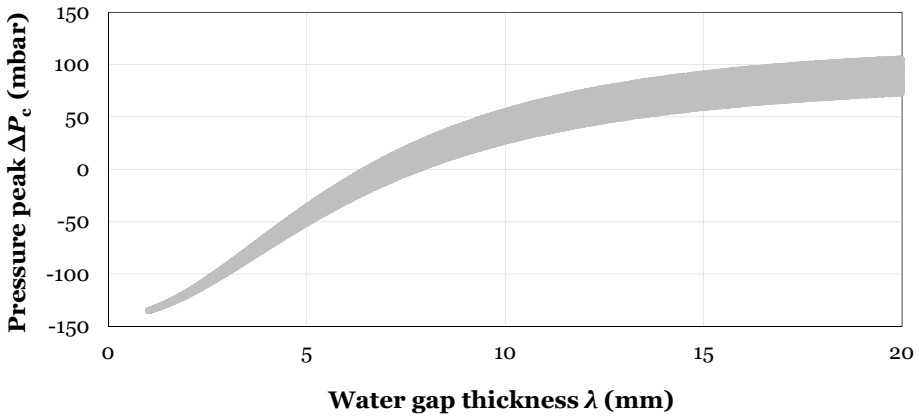

Figure 22 – Pressure peak term ΔP_c obtained by Model 2 when varying λ and C_g only

Fig. 22 depicts the variance of ΔP_c obtained with Model 2 when varying λ and C_g only. One can notice that ΔP_c is either positive of negative according to the flow rate value in each branch. Thus, zero values obtained for λ around 7 mm correspond to equal velocities through the grid and the water gap (as shown by Eq. 13), which means a uniform flow. The dispersion induced by C_g clearly increases as the thickness λ grows larger. The Sobol indexes associated to this sensitivity analysis are given in Fig. 23.

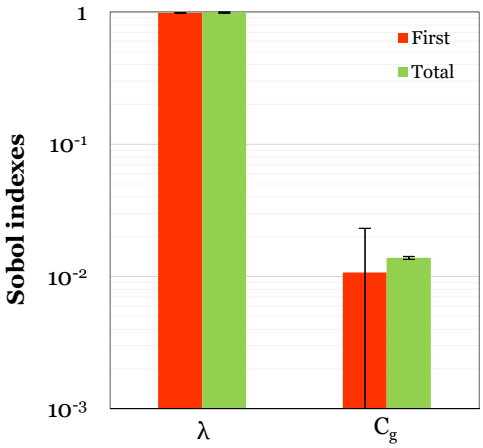

Figure 23 – Sobol indexes and 95% confidence intervals for ΔP_c obtained with 100 000 calculations with Model 2 in the context of real PWR fuel assemblies

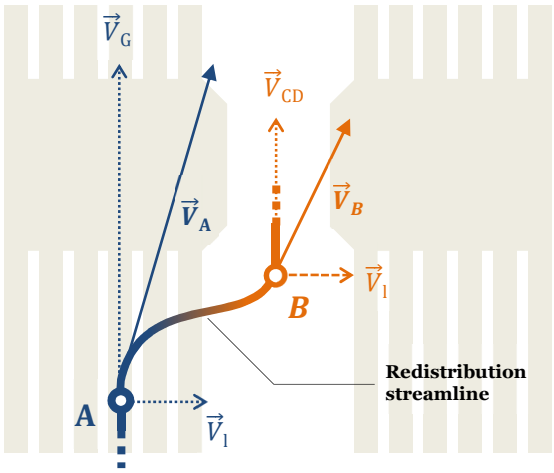

Figure 24 - Streamline upstream from the CD with fuel rods

In the case of Model 3, the quantity of interest is $\Delta P_{tot} = \Delta P_c + \Delta P_l$. Indeed, two effects are now are involved in the upstream pressure drop. This can be shown by applying the generalized Bernoulli principle on a streamline following the flow redistribution (Fig. 24) for instance from the grid (point A, velocity $\vec{V}_A = \vec{V}_g + \vec{V}_l$ and pressure $P_A = P_g$) to the water gap (point B, velocity $\vec{V}_B = \vec{V}_{cd} + \vec{V}_l$ and pressure $P_B = P_{cd}$). The sign convention for ΔP_l comes from Eq. 24:

$$P_A + \frac{1}{2}\rho V_A^2 = P_B + \frac{1}{2}\rho V_B^2 - \Delta P_l \qquad \text{(Eq. 28)}$$

which leads to the following formula for the total pressure drop:

$$\Delta P_{AB} = P_{cd} - P_g = \frac{1}{2}\rho\left(V_g^2 - V_{cd}^2\right) + \Delta P_l = \Delta P_{tot} \qquad \text{(Eq. 29)}$$

(to be compared to Eq. 13 which gives $P_{cd} - P_g = \Delta P_c$ in the case of Model 2).

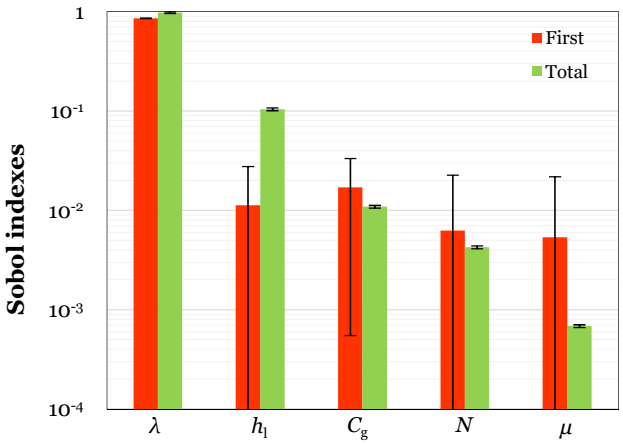

Figure 25 - Sobol indexes and 95% confidence intervals for ΔP_{tot} obtained with 100 000 calculations with Model 3 in the context of real PWR fuel assemblies

Fig. 25 highlights Sobol indexes obtained for ΔP_{tot}. Once again, λ has by far the highest effect among all inputs. But in this new situation, the sum of all first indexes is not equal to 1, meaning that correlations exist between inputs. From h_l indexes, it can be inferred that this input is unimportant alone but has a significant impact through interactions, most probably with λ.

In order to grasp a better understanding of the roles of λ and h_l, the same calculations have been performed considering all the other inputs as constants with nominal values. Quantities of interest such as ΔP_c and ΔP_{tot} can therefore be visualized with smooth curves (instead of fuzzy scatter plots like in Fig. 22 for instance). Fig. 26 shows the evolution of Model 3 outputs along with h_l (for different values of λ) whereas Fig. 27 and 28 show their evolution along with λ (for different values of h_l).

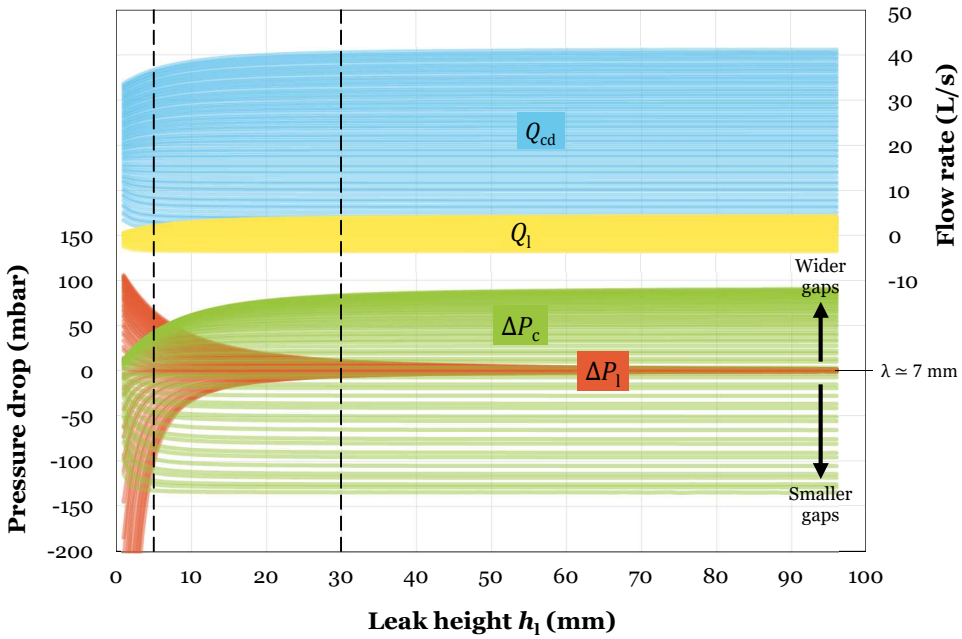

Figure 26 - Evolution of the flow rates and pressure drops along with h_l for different values of λ

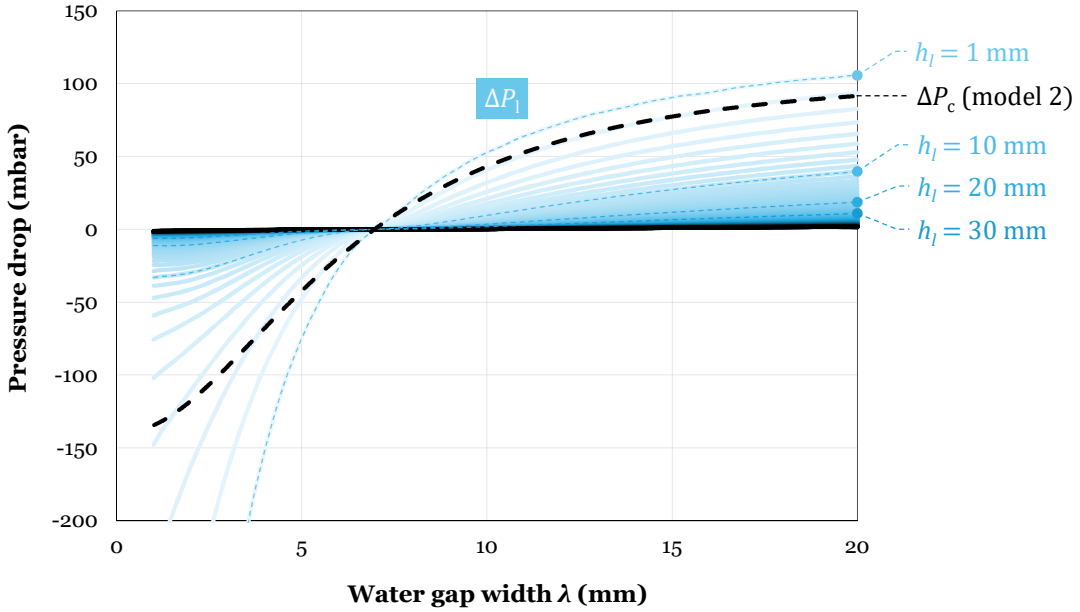

Figure 27 - Evolution of the lateral pressure drop along with λ for different values of h_l

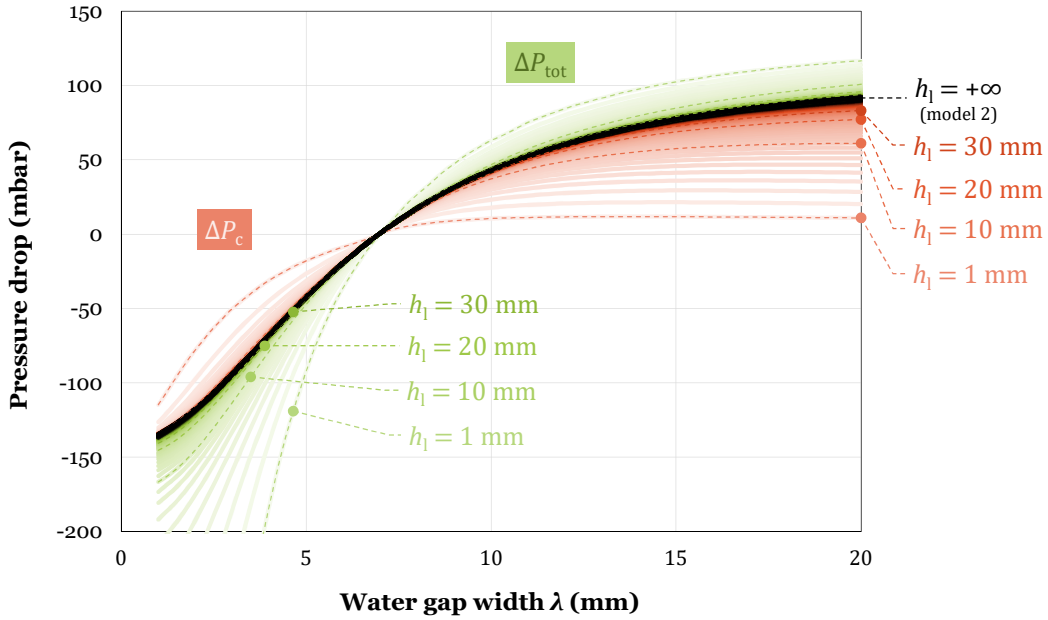

Figure 28 - Evolution of the upstream pressure drop along with λ for different values of h_l

One first observation is the presence of a singular point when both λ and h_l approch zero, for which the upstream pressure drop ΔP_{tot} associated to the redistribution becomes potentially infinite. Actually, the singular term is rather ΔP_l. It makes sense because that singular point correspond to a situation where almost all the incoming flow would be forced towards the grids ($\lambda \simeq 0$) by going through an extremely thin horizontal slit ($h_l \simeq 0$). Hence, care must be taken so as not to choose too small a value for the h_l parameter. We suggest to keep h_l above 5 mm at the very least.

On the contrary, when h_l grows larger, Fig. 26 and 27 show that ΔP_l approach zero whatever the value of λ. In other words, Model 3 asymptotically tends towards Model 2 when h_l becomes infinite.

Actually, it is possible to observe on Fig. 26 that the evolutions of flow rates and pressure drops become somewhat unaffected by increasing h_l beyond 3 cm.

The *loci* where pressure drop curves of Fig. 27 and 28 cross the horizontal axis is almost a single point near $\lambda \simeq 7$ mm. When the water gap has this width, the axial flow profile is flat ($V_{cd} = V_g$, with no cross-flow). Since it hardly depends on h_l at all, even Model 2 or a poorly calibrated Model 3 would be able to predict this equilibrium value accurately.

For intermediate values of h_l (in the "reasonable range" between 5 mm and 3 cm), one can wonder how the redistribution term of Model 2, namely ΔP_c, blends in the one of Model 3, namely $\Delta P_{tot} = \Delta P_c + \Delta P_l$. For h_l between 5 and 30 mm, Fig. 27 shows that the additional term ΔP_l increases (in absolute value) when h_l gets smaller, staying below the asymptotic value of ΔP_c curve for Model 2 even so. Conversely, Fig. 28 shows that ΔP_c decreases (in absolute value) along with h_l, but not enough to compensate for the additional upstream pressure drop brought by ΔP_l. Everyting boils down in the end to the total pressure drop ΔP_{tot} being slighted increased (in absolute value) when the length h_l becomes smaller. One worthy observation is that the flow rate Q_{cd} in the water gap shows little dependence on h_l. These results are the very purpose of Model 3 enhancements versus Model 2, aimed at tweaking the pressure axial profile without jeopardizing the good prediction of the flow rate redistribution, which was already validated for Model 2 by comparison to DIVA+G experimental data.

CONCLUSION AND OPEN PROSPECTS

In this article, a series of different 1D hydraulic models of growing complexity were introduced to reproduce the flow redistribution upstream from the grids for two fuel assemblies separated by a water gap. All models are based on hydraulic networks, starting from the simple association of two pathways: one for the bypass, and one for the grids. The first model does not take into account the pressure peak which appears when the bypass is being closed, yielding a second model containing a modified energy equation to consider the effects of the identified stagnation point. Finally, a third model adds the lateral hydraulic resistance of the fuel rods, to further increase the accuracy of the network for small water gaps.

Although Model 1 turns out to be far too simplistic, both Model 2 and Model 3 are well-suited for reproducing the CFD results obtained with TrioCFD and Code_Saturne, with excellent agreement achieved by Model 3 even in the case of very narrow bypasses. Models 1 and 2 were also compared to a dedicated experiment called DIVA+G consisting in two 3D-printed porous grids facing each other, between which is located a bypass of variable thickness. Model 3 was not relevant in this case as there is no rod bundle in the mock-up. Model 2 accurately predicted flow rates and pressure losses measured in DIVA+G, validating the global strategy proposed to account for the flow redistribution upstream from the grids. As regards the improvements brought in Model 3 to account for the lateral obstruction due to the fuel rods, sensitivity analyses suggest that a particular attention should be paid to the choice of the h_l parameter, due to its significant influence on the pressure drop. Relying on CFD simulations is recommended to assess its value, with some insights given in the present paper. Dedicated LES calculations are considered in the future to consolidate the results of the proposed k-ε validation cases.

The next step of this work consists in building a model for the lateral forces acting on the fuel assembly resulting from the computed flow rates and pressures. This will be followed by the construction of extended models involving hydraulic networks and fluid-structure interaction, first to represent a 2D row of assemblies separated by water gaps, and second to test a 3D arrangement of assemblies close to a full PWR core. These prospects are supported by the capability of the proposed

687 approach to carry out extended sensitivity analyses thanks to the computational efficiency of the semi-
688 analytical expression of the hydraulic networks. The final objective lies in identifying relevant patterns
689 related to flow redistribution with fluid-structure interaction, so as to draw some guidelines to improve
690 existing models involving classical porous approximations.

691 **ACKNOWLEDGEMENTS**

692 The authors would like to thank the TrioCFD team and the code's maintenance at the CEA's Fluid
693 Mechanics and Thermal Hydraulics Service for all the necessary support lent to this work.

694 **REFERENCES**

695 **Andersson, T. & al. (2004).** A decade of assembly bow management at Ringhals. *IAEA-TECDOC-*
696 *1454 Structural Behaviour of Fuel Assemblies for Water Cooled Reactors, Vienna, Austria (2005).*
697 **Angeli, P-E & al. (2015)**. Overview of the TrioCFD code: main features, V&V procedures and typical
698 applications to nuclear engineering. *NURETH-16, Chicago, IL, August 30-September 4*
699 **Archambeau, F. (2004)**. Code_Saturne: A Finite Volume Code for the computation of turbulent
700 incompressible flows – Industrial Applications. *International Journal on Finite Volumes.*
701 **Asker, M. & al (2014)**. A review of non iterative friction factor correlations for the calculation of
702 pressure drop in pipes. *Journal of Science and Technology*. (4) 1, 1-8.
703 **Benra, F.-K. (2011)**. A Comparison of One-Way and Two-Way Coupling Methods for Numerical
704 Analysis of Fluid-Structure Interactions. *Journal of Applied Mathematics*, vol. 2011, 1-16.
705 **Bieder, U. (2012)**. Analysis of the flow down-and upwind of split-type mixing vanes. *OCDE*
706 *Workshop CFD4NRS-4, Daejeon, South Korea, 10–12 September.*
707 **Bieder, U. (2014)**. LES analysis of the flow in a simplified PWR assembly with mixing grid. *Progress*
708 *in Nuclear Energy, 75, 15-24.*
709 **Bieder, U. (2015a)**. CFD analysis of the flow in the near wake of a generic PWR mixing grid. *Annals*
710 *of Nuclear Energy, Vol. 82, pp 169-178.*
711 **Bieder, U. (2015b)**. CFD Analysis of Non-Axial Flow in Fuel Assemblies. *NURETH-16, Chicago, IL,*
712 *August 30-September 4.*
713 **Bieder, U. (2020)**. CFD analysis of intra and inter fuel assembly mixing. *Annals of Nuclear Energy,*
714 *Vol. 135, Article Number 106977.*
715 **Cross, H. (1936)**. Analysis of Flow in Networks of Conduits or Conductors. *University of Illinois*
716 *Bulletin. Vol. 34, No. 22.*
717 **de Lambert, S. & al (2019)**. Modeling the consequences of fuel assembly bowing on PWR core
718 neutronics using a Monte-Carlo code. *Annals of Nuclear Energy, Vol. 134, December 2019, pages*
719 *330-341.*
720 **Gaudier, F. (2010)**. URANIE: The CEA/DEN Uncertainty and Sensitivity platform. *Procedia –*
721 *Social and Behavorial Sciences, Vol. 2, No. 6, pages 7660-7661.*
722 **Gabrielsson, P. & al. (2018)**. Investigation of the development of fuel assembly bow in Ringhals 3
723 and 4. *Top Fuel Reactor Fuel Performance 2018, 30 September – 04 October, Prague, Czech*
724 *Republic.*
725 **Horváth, Á. & Dressel, B. (2013)**. On numerical simulation of fuel assembly bow in pressurized
726 water reactors. *Nuclear Engineering and Design, vol. 265, pages 814-825.*
727 **IAEA (2010)**. Review of Fuel Failures in Water Cooled Reactors. IAEA Nuclear Energy Series NF-T-
728 2.1.
729 **Idel'cik, I.E. (1986)**. Mémento des pertes de charges. *Eyrolles, EDF. Direction des études et*
730 *recherches d'Electricité de France (EDF).*
731 **Iooss, B. (2011).** *Revue sur l'analyse de sensibilité globale de modèles numériques*. Journal de la
732 Société Française de Statistique, Vol. 152, No. 1.
733 **Jacques, J. (2006).** *Sensitivity analysis in presence of model uncertainty and correlated inputs.*
734 Reliability Engineering & System Safety, Vol. 91, Issues 10-11, Oct-Nov 2006, pages 1126-1134.
735 **Jacques, J. (2011).** *Pratique de l'analyse de sensibilité : comment évaluer l'impact des entrées*
736 *aléatoires sur la sortie d'un modèle mathématique*. PUB. IRMA, Vol. 71, N° III.
737 **Lascar, C. (2015)**. Advanced predictive tool for fuel assembly bow based on a 3D coupled FSI
738 approach. *Top Fuel Reactor Fuel Performance 2015, 13-17 September 2015, Zurich, Switzerland.*

McKay, M.D. & al. (1979). A Comparison of Three Methods for Selecting Values of Input Variables in the Analysis of Output from a Computer Code. *Technometrics, Vol. 21, No. 2, pp. 239-245.*

Moody, L.F. (1944). Friction Factors for Pipe Flow. *Transactions of the ASME. vol. 66, pages 671-684.*

Nielsen, H.B. (1989). Methods for Analyzing Pipe Networks. *Journal of Hydraulic Engineering. vol. 115, pages 139-157.*

Peybernès, J. (2005). Evaluation of the forces generated by cross-flow on PWR fuel assembly. *IAEA-TECDOC-1454 Structural Behaviour of Fuel Assemblies for Water Cooled Reactors, Vienna, Austria (2005).*

Puragliesi, R. & al. (2019). Comparison of Computational Fluid Dynamics and Subchannel Numerical Solutions of Fuel Assemblies Characterised by Bowing. 18th International Topical Meeting on Nuclear Reactor Thermal Hydraulics (NURETH-18), August 18-23, Portland, USA.

Rennels, D. C. & Hudson H. M. (2012). *Pipe Flow: A Practical and Comprehensive Guide*. John Wiley & Sons, Inc.

Ricciardi G. & al. (2009). Row of fuel assemblies analysis under seismic loading: Modelling and experimental validation. Nuclear Engineering and Design, vol. 239, issue 12, pages 2692-2704.

Ricciardi G. & Boccaccio, E. (2014). Measurements of fluid fluctuations around an oscillating nuclear fuel assembly. *Journal of Fluids and Structures, Vol. 48, pages 332-346.*

Ricciardi G. & Boccaccio, E. (2015). Modelling the flow induced stiffness of a PWR fuel assembly. *Nuclear Engineering and Design, Vol. 282, pages 8-14.*

Ruiz Antón-Pacheco, J. G. (2017). Study of the set up of a fluid structure coupling interface (FSI) between PWR fuel assemblies and the reactor coolant. *Master's thesis, Universitat Politècnica de València, Escuela Técnica Superior de Ingenieros Industriales Valencia.*

Stabel, J. (2011). Advanced methodology to predict in-reactor bow of PWR fuel assemblies for efficient design optimization: Background, Validation, Examples. *Light Water Reactor Fuel Performance Meeting, Chengdu, China, September 11-14, 2011.*

Wanninger, A. & al. (2016). Screening sensitivity analysis of a PWR fuel assembly FEM structural model. TopFuel 2016, September 11-16, Boise, USA.

Wanninger, A. & al. (2018). Mechanical analysis of the bow deformation of a row of fuel assemblies in a PWR core. *Nuclear Engineering and Technology, Vol. 50, pages 297-305.*

Wood, D.J. & Charles, C.O.A (1972). Hydraulic Network Analysis Using Linear Theory. *Journal of the Hydraulics Division, ASCE. Vol. 98, pp 1157-1170.*

Wood, D.J. & Rayes, A.G. (1981). Reliability of algorithms for pipe network analysis. *Journal of the Hydraulics Division, ASCE. vol. 107, pages 1145-1161.*

Xu, T. & al. (2019). Numerical simulation of fuel assembly deformation induced by flow redistribution with Code_Saturne. 18th International Topical Meeting on Nuclear Reactor Thermal Hydraulics (NURETH-18), August 18-23, Portland, USA.

Yan, J. & al. (2014). Influence of Spacer Grid Outer Strap on Fuel Assembly Thermal Hydraulic Performance. *Science and Technology of Nuclear Installations, Vol. 2014, Article ID 602062, 9 pages.*